

Hybrid high-resolution RBF-ENO method

Jan S. Hesthaven, Fabian Mönkeberg*

SB-MATH-MCSS, École Polytechnique Fédérale de Lausanne (EPFL), 1015 Lausanne, Switzerland



ARTICLE INFO

Article history:

Received 14 July 2020

Received in revised form 25 November 2020

Accepted 21 March 2021

Available online 24 March 2021

Keywords:

Finite volume method

Hybrid grids

Radial basis functions

ENO reconstruction

Positivity preserving method

Conical aerospike nozzle

ABSTRACT

Essentially nonoscillatory (ENO) and weighted ENO (WENO) methods on equidistant Cartesian grids are widely used to solve partial differential equations with discontinuous solutions. The RBF-ENO method is highly flexible in terms of geometry, but its stencil selection algorithm is computationally expensive. In this work, we combine the computationally efficient WENO method and the geometrically flexible RBF-ENO method in a hybrid high-resolution essentially nonoscillatory method to solve hyperbolic conservation laws. The scheme is based on overlapping patches with ghost cells, the RBF-ENO method for unstructured patches and a standard WENO method on structured patches. Furthermore, we introduce a positivity preserving limiter for non-polynomial reconstruction methods to stabilize the hybrid RBF-ENO method for problems with low density or pressure. We show its robustness and flexibility on benchmarks and complex test cases such as the scramjet inflow problem and a conical aerospike nozzle jet simulation.

© 2021 The Authors. Published by Elsevier Inc. This is an open access article under the CC BY license (<http://creativecommons.org/licenses/by/4.0/>).

1. Introduction

Hyperbolic conservation laws attract substantial interest in science and engineering. They model the dynamics of systems of conserved quantities and are expressed as the system of equations

$$\mathbf{u}_t + \sum_{i=1}^d f_i(\mathbf{u})\mathbf{x}_i = 0, \quad (\mathbf{x}, t) \in \mathbb{R}^d \times \mathbb{R}_+, \quad (1)$$

$$\mathbf{u}(0) = \mathbf{u}_0,$$

with the initial conditions $\mathbf{u}_0: \mathbb{R}^d \rightarrow \mathbb{R}^N$, the conserved variables $\mathbf{u}: \mathbb{R}^d \times \mathbb{R}_+ \rightarrow \mathbb{R}^N$, e.g., mass, momentum, and energy, and the flux functions $f_i: \mathbb{R}^N \rightarrow \mathbb{R}^N$. One possible method to solve (1) is the finite volume method, which is based on a discretization of the domain into polyhedral cells $C_i \subset \mathbb{R}^d$, and is derived by integrating over a cell C_i , dividing by its size and applying the divergence theorem to recover

$$\frac{dU_i}{dt} = -\frac{1}{|C_i|} \int_{\partial C_i} f(\mathbf{u}(\mathbf{s}, t)) \cdot \mathbf{n}(\mathbf{s}) \, ds. \quad (2)$$

Here we have the outwards pointing normal vector $\mathbf{n}(\mathbf{s})$, $f = (f_1, \dots, f_d)$ and the cell average

* Corresponding author.

E-mail address: fm@moenkeberg.ch (F. Mönkeberg).

$$U_i = \frac{1}{|C_i|} \int_{C_i} \mathbf{u}(\mathbf{x}, t) d\mathbf{x}. \quad (3)$$

Thus, the change of the conserved variables over time in the cell C_i is described by the flux through its boundary. By splitting the boundary integral (2) into its faces C_{il_e} , we obtain the semi-discrete scheme

$$\frac{dU_i}{dt} = -\frac{1}{|C_i|} \sum_{l_e=1}^{n_i} F_{il_e}, \quad (4)$$

with the numerical flux

$$F_{il_e} = \int_{\partial C_{il_e}} f(\mathbf{u}(\mathbf{s}, t)) \cdot \mathbf{n}_{il_e} d\mathbf{s} + \mathcal{O}(\Delta x^p), \quad (5)$$

for $p \geq 1$, ∂C_{il_e} the edge between cell C_i and its l_e th neighbor, and the outward pointing normal vector \mathbf{n}_{il_e} to the interface ∂C_{il_e} . Common first order numerical fluxes are of the form $F_{il_e} = F_{il_e}(U_i, U_{il_e}, \mathbf{n}_{il_e})$, e.g., the Rusanov flux

$$F_{il_e}^R(U, V, \mathbf{n}_{il_e}) = \frac{|\partial C_{il_e}|}{2} (f(U) + f(V)) \cdot \mathbf{n}_{il_e} - \frac{\alpha_{il_e}(U, V) |\partial C_{il_e}|}{2} (V - U), \quad (6)$$

with

$$\alpha_{il_e}(U, V) = \max\{\lambda_{\max}(\nabla_{\mathbf{u}} f(U) \cdot \mathbf{n}_{il_e}), \lambda_{\max}(\nabla_{\mathbf{u}} f(V) \cdot \mathbf{n}_{il_e})\}, \quad (7)$$

and the Jacobian $\nabla_{\mathbf{u}} f$ of f in \mathbf{u} and the maximum eigenvalue $\lambda_{\max}(A)$ of a matrix A . We can apply an arbitrary time discretization technique to recover a fully discrete scheme from (4), e.g., a strong stability preserving Runge-Kutta method [1]. Using the explicit Euler method we receive the well-known fully discrete scheme in conservative form

$$U_i^{n+1} = U_i^n - \frac{\Delta t}{|C_i|} [F_{i+1/2}^n - F_{i-1/2}^n], \quad (8)$$

where $U_i^n \approx U_i(t^n)$, $\Delta t = t^{n+1} - t^n$ and $F_{i+1/2}^n = F(U_i^n, U_{i+1}^n)$.

To generate a high-order finite volume method we need to approximate the boundary integral with a high order quadrature rule and approximate the flux at each quadrature point in a high-order manner. One way to generate a high-order approximation of the flux is the MUSCL approach [2]. The idea is to construct a high-order reconstruction $s_i : \mathbb{R}^d \rightarrow \mathbb{R}$ for each cell C_i , that interpolates the solution in a mean value sense on the stencil S_i , and to evaluate the first order flux at each quadrature node using these reconstructions. To formalize the idea we introduce the averaging operator

$$\lambda_C(f) = \frac{1}{|C|} \int_C f(\mathbf{x}) d\mathbf{x}, \quad (9)$$

for a function $f : \mathbb{R}^d \rightarrow \mathbb{R}$ and a domain $C \subset \mathbb{R}^d$. The interpolation problem with average values can be written as

$$\lambda_C s_i = U_C, \quad \text{for all } C \in S_i, \quad (10)$$

with the average value U_C of the cell C . A high-order boundary integral approximation of (5) and the high-order accurate reconstruction s_i of the local solution are used to evaluate the first order flux $F(U, V, \mathbf{n}_{il_e})$ on the quadrature points. This high-order flux can be written as

$$F_{il_e} = \sum_{k=1}^{n_Q} \omega_k F_{il_e}^R(s_i(\mathbf{x}_k), s_{il_e}(\mathbf{x}_k), \mathbf{n}_{il_e}), \quad (11)$$

with the quadrature weights ω_k , the quadrature points \mathbf{x}_k for $k = 1, \dots, n_Q$ with the number of quadrature points $n_Q \in \mathbb{N}$, the high-order accurate reconstruction s_i and s_{il_e} of the solutions for the cell C_i and for its l_e th neighbor, respectively.

However, the choice of the stencil S_i is not trivial. The interpolation procedure can introduce artificial oscillations which destabilize the scheme. Such spurious oscillations, that occur at discontinuities, are a well-known problem for high-order linear methods, referred to as the Gibbs phenomenon [3]. It can only be avoided by using nonlinear schemes. To address this Harten et al. [4] proposed the essentially nonoscillatory (ENO) scheme based on the MUSCL approach. This method reduces the oscillations that occur due to the interpolation step by choosing the stencil with the least oscillatory behavior, see Fig. 1. To choose the least oscillatory stencil there exist different options. The stencil choice of the original method for one-dimensional equations is based on the divided differences for polynomials. Thus, the degree p of the reconstruction is based on the reconstruction with stencils of size $n = p + 1$. This concept was extended to multidimensional domains on

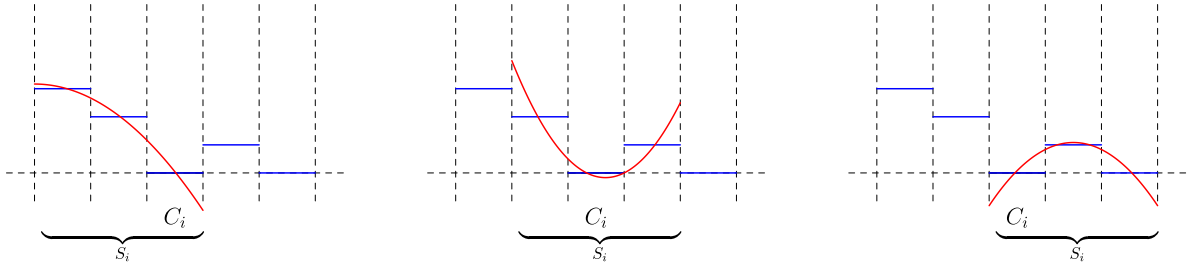


Fig. 1. Different stencils and its reconstruction with $n = 3$.

general grids [5,6]. Liu et al. [7] introduced the weighted ENO (WENO) method which allows to obtain even higher order of convergence with similar computational complexity by using convex combinations of solutions computed on different stencils from the ENO method.

The classic approaches are based on polynomial interpolation. While polynomial interpolation is well understood in one spatial dimension, it poses some challenges in higher dimensions. In the case of unstructured grids, we must face the problem of (unique) solvability of the interpolation system. To resolve this problem, we replace the polynomials with radial basis functions (RBFs). The concept of RBFs was introduced by Hardy to solve general interpolation of scattered data in two dimensions [8] and found application in different domains [9]. Later, multiple methods based on RBFs were developed to solve partial differential equations, e.g., collocation techniques, variational formulations and boundary element methods based on RBFs [10] and the RBF-FD method [11,12]. Furthermore, there are already several other approaches that combine radial basis functions (RBF) with finite volume methods, e.g., [13–20]. The two-dimensional RBF-ENO method introduced in [21] uses RBFs to increase the stability and the flexibility with unstructured grids. However, this method suffers from an expensive stencil selection algorithm. In this work, we introduce a hybrid high-resolution ENO method which combines the geometrically flexible RBF-ENO method [21] with the efficient standard two-dimensional WENO method [22].

In Section 2, we introduce the methods on which the hybrid scheme is based on, e.g., the radial basis function interpolation based on cell averages, the WENO and the RBF-ENO method. Section 3 defines the hybrid high-resolution RBF-ENO method, which reduces the computational complexity in the structured parts of the grid, and Section 4 describes a generalized version of the maximum preserving limiter from [23]. In Section 5, we verify numerically the method including two challenging examples: the scramjet inflow problem and the conical aerospike jet simulation. Section 6 summarizes the results.

2. Computational methods

In this section, we introduce the different elements used to construct the hybrid high-resolution RBF-ENO method.

2.1. Radial basis functions

Radial basis functions (RBF) were introduced for function approximation on scattered data. Their mesh-free property, their geometric flexibility and their direct generalization to high dimensions often make them advantageous as compared to alternatives. Based on the seminal work by Hardy [8], Duchon [24], and Micchelli [25], RBFs have achieved considerable results, especially in the field of computational geoscience. The interested reader is referred to [9] to find some more recent results.

To apply RBFs in the finite volume framework, we follow the approach in [15,16] based on cell averages. The idea is to use the average over the cells of a single univariate continuous function $\phi : \mathbb{R} \rightarrow \mathbb{R}$, the *radial basis function*, composed with the Euclidean norm augmented with a polynomial

$$s(\mathbf{x}) = \sum_{i=1}^n a_i \lambda_{C_i}^{\xi} \phi(\mathbf{x} - \xi) + p(\mathbf{x}), \quad p \in \Pi_{l-1}(\mathbb{R}^d), \quad (12)$$

with $\lambda_C^{\xi} f$ being the average operator of f over the cell C with respect to the variable ξ . Because of the augmentation with the polynomial, the interpolation problem (10) must be extended as

$$\lambda_{C_j} s = U_j, \quad \text{for all } j = 1, \dots, n, \quad (13a)$$

$$\sum_{i=1}^n a_i \lambda_{C_i}(q) = 0, \quad \text{for all } q \in \Pi_{l-1}(\mathbb{R}^d). \quad (13b)$$

To discuss about well-posedness of (13), we introduce the definition of conditionally positive definite radial basis functions of order l .

Table 1

Commonly used RBFs with $\mathbb{N} \ni \nu > 0, k \in \mathbb{N}$ and $\varepsilon > 0$.

RBF	$\phi(r)$	Order
Infinitely smooth RBFs		
Multiquadratics	$(1 + (\varepsilon r)^2)^\nu$	$\lceil \nu \rceil$
Inverse multiquadratics	$(1 + (\varepsilon r)^2)^{-\nu}$	0
Gaussians	$\exp(-(\varepsilon r)^2)$	0
Piecewise smooth RBFs		
Polyharmonic Splines	r^{2k-d}	k
	$r^{2k-d} \log(r)$	k

Definition 2.1 (Conditionally positive definite function). A function $\phi : \mathbb{R}^d \rightarrow \mathbb{R}$ is called conditionally positive (semi-) definite of order l if for any pairwise distinct points $\mathbf{x}_1, \dots, \mathbf{x}_n \in \mathbb{R}^d$ and $c = (c_1, \dots, c_n)^T \in \mathbb{R}^n \setminus \{0\}$ such that

$$\sum_{i=1}^n c_i p(\mathbf{x}_i) = 0, \tag{14}$$

for all $p \in \Pi_{l-1}(\mathbb{R}^d)$, the quadratic form

$$\sum_{j,k=1}^n c_j c_k \phi(\mathbf{x}_j - \mathbf{x}_k), \tag{15}$$

is positive (non-negative).

Let us consider a conditionally positive definite radial basis function ϕ and a set $\{\lambda_{C_i}\}_{i=1}^n$ which is $\Pi_{l-1}(\mathbb{R}^d)$ -unisolvent with $n \in \mathbb{N}$, i.e., for $p \in \Pi_{l-1}(\mathbb{R}^d)$ it holds

$$\lambda_{C_i} p = 0 \quad \text{for } i = 1, \dots, n \quad \Rightarrow p = 0. \tag{16}$$

Then, (13) has a unique solution [14]. The most commonly used RBFs are listed in Table 1, all of which are conditionally semi-positive definite or semi-negative definite. A RBF ϕ is called conditionally semi-negative if $-\phi$ is conditionally semi-positive.

2.2. Standard WENO method

The ENO method considers $2n - 1$ cells to recover a reconstruction of degree $n - 1 \in \mathbb{N}$ on a stencil of size n and a finite volume method of order $p = n$. However, by using $2n - 1$ cells the maximum degree we can hope for in the smooth case is $2n - 2$ and a finite volume method of order $p = 2n - 1$. Liu et al. [7] introduced the weighted ENO method based on the use of a convex combination of the solutions s_i^j of each stencil $S_i^j = \{C_{i-j}, \dots, C_{i-j+n-1}\}$ for each $j = 0, \dots, n - 1$ to create a stable finite volume method of order $p = 2n - 1$.

Given $s_i^j : \mathbb{R} \rightarrow \mathbb{R}$ such that

$$\lambda_C s_i^j = U_C, \quad \text{for all } C \in S_i^j, \text{ for each } j = 0, \dots, n - 1, \tag{17}$$

we define the reconstruction

$$s_i(x) = \sum_{j=0}^{n-1} \omega_i^j s_i^j(x), \tag{18}$$

such that $\omega_i^j = d_i^j + \mathcal{O}(\Delta x^{n-1})$ in smooth regions with the coefficients $d_i^j \in \mathbb{R}$ fulfilling

$$s_{i\pm 1/2}^\mp = \sum_{j=0}^{n-1} d_i^j s_i^j(x_{i\pm 1/2}) = u(x_{i\pm 1/2}) + \mathcal{O}(\Delta x^{2n-1}). \tag{19}$$

The convexity property $\sum_{j=0}^{n-1} \omega_i^j = 1$ with $\omega_i^j \geq 0$ is needed for consistency and stability. A popular choice for the nonlinear coefficients ω_i^j was proposed by Jiang and Shu [22]

$$\omega_i^j = \frac{\alpha_i^j}{\sum_{i_0=0}^n \alpha_i^{i_0}}, \quad \alpha_i^j = \frac{d_i^j}{(IS_{C_i}[S_i^j] + \bar{\varepsilon})^t}, \tag{20}$$

where $\bar{\varepsilon} \ll 1$ and the smoothness indicator $IS_C : C^\infty(\mathbb{R}) \rightarrow \mathbb{R}$ which measures the smoothness of the reconstruction. To preserve the right order of accuracy in the smooth case we require

$$IS_C[s] = C(\Delta x)(1 + \mathcal{O}(\Delta x^{n-1})). \tag{21}$$

In the case of a non-smooth function, we need

$$IS_C[s] = \mathcal{O}(1). \tag{22}$$

In comparison with the ENO method one of the main additional challenges of the WENO method is the choice of the coefficients d_j^i , especially for unstructured grids. To solve multidimensional problems, there exists dimensional splitting to solve multidimensional problems with one-dimensional methods [26]. However, applying the dimensional splitting with high-order finite volume schemes does not directly result in a high-order method, but rather in a high-resolution method. To recover the right order of convergence the flux must be calculated for each quadrature point on the boundary of the quadrilateral. More information and analysis can be found in [22,27].

2.3. RBF based ENO method

To solve the conservation law on general grids we use the two-dimensional RBF-based ENO method, which was introduced in [21]. The method uses the high-order finite volume method from Section 1 with the numerical flux (11) and the RBF reconstruction (12) based on the multiquadratic spline of first order.

To choose the stencil for a two-dimensional grid, we use Algorithm 2.1 with the general smoothness indicator [20]

$$IS_{RBF}(s) := \sum_{i=1}^n a_i^2, \tag{23}$$

for the reconstruction $s(\mathbf{x}) = \sum_{i=1}^n a_i \lambda_{C_i}^\xi \phi(\mathbf{x} - \xi) + \sum_{j=1}^m b_j p_j(\mathbf{x})$ with the polynomials $p_j \in \Pi_l(\mathbb{R}^2)$ of maximal degree l . To

Algorithm 2.1 Recursive RBF stencil selection algorithm for multiple dimensions.

Let the interpolation cells $S_i = \{C_{i_1}, \dots, C_{i_k}\}$ and its mean-values U_{i_1}, \dots, U_{i_k} be given.

Let $N_i = \{C_{j_0}, \dots, C_{j_l}\}$ be the direct neighbors for all $C \in S_i$ such that $N_i \cap S_i = \emptyset$.

Start by initializing $S_i := \{C_i\}$ and $N_i := \{C \mid C \text{ is neighbor of } C_i\}$.

for $j = 0, \dots, n - 2$ **do**

 Set $S_{j_s} := S_i \cup \{C_{j_s}\}$ for all $s = 1, \dots, l$ and $C_{j_s} \in N_i$.

$r := \operatorname{argmin}_s IS_{RBF}(S_{j_s})$

$S_i := S_i \cup \{C_{j_r}\}$

$N_i := N_i \cup \{C \notin S_i \mid C \text{ is neighbor of } C_{j_r} \text{ and } d(C) \leq d_{max}\} \setminus \{C_{j_r}\}$

end for

circumvent stability issues, we must choose the right polynomial degree for each stencil and the right shape parameter. For a given stencil of size n we pick the polynomial degree

$$l = \begin{cases} \lfloor -2.5 + \frac{1}{2}\sqrt{1 + 8(n-1)} \rfloor, & n \geq 5, \\ 0 & n < 5. \end{cases} \tag{24}$$

Thus, we have slightly more cells than optimally needed in the polynomial case, i.e.,

$$n = \frac{(l+2)(l+1)}{2} \iff l = -1.5 + \frac{1}{2}\sqrt{1 + 8n}, \tag{25}$$

which reduces the probability of having an ill-conditioned stencil. By choosing the shape parameter as

$$\varepsilon = \frac{1}{\sqrt{|C_i|}}, \tag{26}$$

we reduce the condition number of the interpolation matrix. Note that in this case the polynomials impose the order of convergence and the RBFs merely stabilize the system of equations. As the polynomial basis we use

$$\left\{ p_i(\mathbf{x}) = \tilde{p}_i(\varepsilon(\mathbf{x} - \tilde{\mathbf{x}})) \mid \text{for } i = 1, \dots, m \right\}, \tag{27}$$

with $\tilde{p}_i \in \{\mathbb{R}^d \rightarrow \mathbb{R}, \mathbf{x} \mapsto x_1^{\alpha_1} \dots x_d^{\alpha_d} \mid \sum_{j=1}^d \alpha_j < l, \alpha_j \in \mathbb{N}\}$, $\deg(\tilde{p}_i) \leq \deg(\tilde{p}_{i+1})$ and $\tilde{\mathbf{x}}$ the incenter of the central cell of the stencil. Note that we denote the central cell as the cell around which we evaluate the boundary integral, i.e., cell C_i of stencil S_i . To restrict the choice of the cells for the stencil and to keep it more compact we define a measure of distance of a cell C to the central cell C_i

Table 2
Stencil setting depending on the polynomial degree l .

Deg. poly. l	1	2	3
n	5	12	30
d_{max}	3	5	8

$$d(C) = 0, \text{ if } C = C_i,$$

$$d(C) = 1, \text{ if } C \text{ is a direct neighbor of } C_i,$$

$$d(C) = 2, \text{ if } C \text{ has a neighbor } \tilde{C} \text{ with } d(\tilde{C}) = 1,$$

...

and $d_{max} \in \mathbb{N}$ as the maximum allowed distance to the central cell. A stable configuration for the RBF-ENO method of order p is given in Table 2 with $l = p - 1$. Note that (24) does not coincide with the values from Table 2. However, from numerical experiments this combination seems superior.

In the one-dimensional case, we compare in Algorithm 2.1 the reconstruction of the stencil S_i with the additional cell on its left to the reconstruction on the stencil S_i with the additional cell to its right. Since in one dimension there is no ill-conditioned stencil, we choose the polynomial degree

$$l = n - 1. \tag{28}$$

Furthermore, we use the shape parameter

$$\varepsilon = \frac{1}{\Delta x}, \tag{29}$$

with Δx the size of the central cell in the stencil. In one dimension this evaluation is stable for $\Delta x \rightarrow 0$ and we conjecture the same for $|C_i| \rightarrow 0$ in two dimensions [21].

Remark 2.1 (*Reconstruction at the boundary*). In one dimension, we use ghost cells at the boundary to enable a high-order reconstruction. In contrast to the one-dimensional version we omit the use of ghost cells for the two-dimensional method. However, we must be aware of the reduced flexibility of the stencil choice in this case. It is known that it is enough to use a method of order $p - 1$ at the boundary to maintain the global formal accuracy [28]. However, in certain cases oscillations appear for all choices of stencils at the boundary. In such cases we do not use a reconstruction for cells directly at the boundary.

3. Hybrid high-resolution RBF-ENO method

In Section 2.3, we presented the RBF-ENO method which is highly flexible in terms of geometry and furthermore ensures high order of accuracy. In this section, we introduce a hybrid high-resolution method based on the standard WENO method on structured grids and the RBF-ENO method on the unstructured parts with the goal to reduce the overall computational cost while maintaining geometric flexibility.

3.1. Hybrid grid generation in one dimension

The basic idea is to split the domain into structured and unstructured parts. Let us take the example in Fig. 2 with the structured part $[a, b]$ and the unstructured part $[b, c]$. In preparation for the two-dimensional case, we denote the unstructured and the structured part as the triangular and the quadrilateral part, respectively. The connection between the different patches is done by using ghost cells. We divide the set of ghost cells into the structured/quadrilateral cells $GHOST_{QUAD}$ and the unstructured/triangular cells $GHOST_{TRI}$. Further, we denote the set of internal cells of the whole grid $INTERNAL$, the set of all edges connected to at least one internal cell Edg , the set of edges at the boundaries such that the cells on their left are outside the patch $Edg_{BC,L}$, and the ones such that the cells on their right are outside the patch $Edg_{BC,R}$. The idea of the hybrid method is to enlarge the domains by $n_{ghost} \in \mathbb{N}$ ghost cells on each side and create the maps

$$f_{TRI} : GHOST_{TRI} \rightarrow INTERNAL, \tag{30}$$

$$f_{QUAD} : GHOST_{QUAD} \rightarrow INTERNAL, \tag{31}$$

to update the ghost cell values in the following way

$$U_i = U_{f_{TRI}(i)}, \quad \text{for all } i \in GHOST_{TRI}, \tag{32}$$

$$U_j = U_{f_{QUAD}(j)}, \quad \text{for all } j \in GHOST_{QUAD}. \tag{33}$$

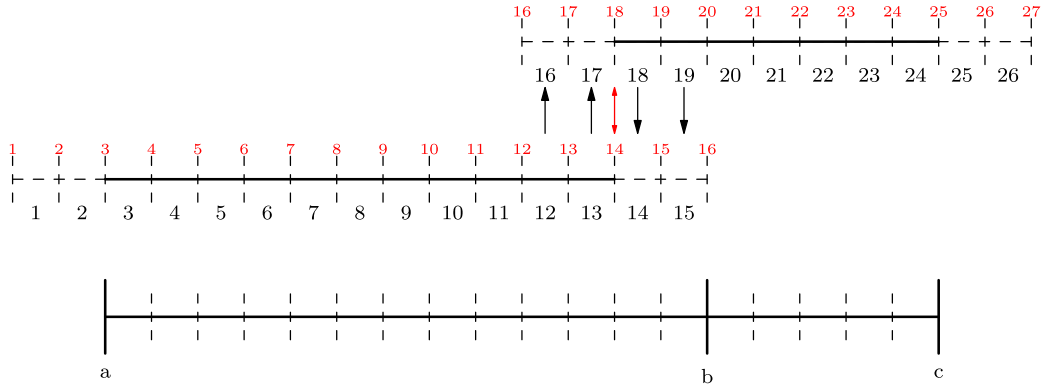


Fig. 2. Principle of 1D hybrid grids with $n_{ghost} = 2$, the black numbers are the labels for the cells and red ones are the labels for the edges.

Example 3.1. Consider the example in Fig. 2. The sets of edges are $Edg = \{3, \dots, 14\} \cup \{18, \dots, 25\}$, $Edg_{BC,L} = \{3, 18\}$ and $Edg_{BC,R} = \{14, 25\}$. The maps to update the ghost cells are given as

$$\begin{aligned} f_{QUAD}(14) &= 18, & f_{TRI}(16) &= 12, \\ f_{QUAD}(15) &= 19, & f_{TRI}(17) &= 13, \end{aligned}$$

and $f_{QUAD}(1), f_{QUAD}(2), f_{TRI}(25), f_{TRI}(26) \in \{3, \dots, 13\} \cup \{18, \dots, 24\}$ depending on the boundary conditions.

Remark 3.1. It is important that we are not directly using the set of structured cells in $[a, b]$ and the unstructured cells in $[b, c]$. To guarantee that the definition of the mappings makes sense, we copy n_{ghost} cells from the structured grid to the neighboring unstructured cells. Thus, the unstructured grid needs to be enlarged by n_{ghost} cells and the size of the structured grid needs to be reduced by n_{ghost} (see Fig. 2).

Now, we are able to apply the WENO method on the structured parts and the RBF-ENO method on the unstructured ones and obtain

$$\begin{aligned} s_i^\pm & \text{ for all } i \in Edg \setminus (Edg_{BC,L} \cup Edg_{BC,R}), \\ s_i^+ & \text{ for all } i \in Edg_{BC,L}, \\ s_i^- & \text{ for all } i \in Edg_{BC,R}. \end{aligned}$$

To obtain the remaining values, we define the maps

$$f_{L2R} : Edg_{BC,L} \rightarrow Edg_{BC,L} \cup Edg_{BC,R}, \tag{34}$$

$$f_{R2L} : Edg_{BC,R} \rightarrow Edg_{BC,L} \cup Edg_{BC,R}, \tag{35}$$

in such a way that for all $i \in Edg_{BC,R}$ and $j \in Edg_{BC,L}$ with $x(i) = x(j)$

$$\begin{aligned} f_{R2L}(i) &= j, \\ f_{L2R}(j) &= i, \end{aligned}$$

with the function $x : Edg \rightarrow \mathbb{R}$ that assigns each edge to its physical position. Thus, we set $s_i^+ = s_{f_{R2L}(i)}^+$ and $s_j^- = s_{f_{L2R}(j)}^-$ for all edges that are not on physical boundary. For edges on the physical boundary these functions depend on the specific boundary conditions. Since each interface i is assigned two values s_i^\pm , we can calculate the numerical flux through each interface and calculate the approximate solution for the next time step.

In Example 3.1, the functions are given as

$$f_{R2L}(14) = 18, \quad f_{L2R}(18) = 14,$$

and $f_{L2R}(3), f_{R2L}(25) \in \{3, 14, 18, 25\}$.

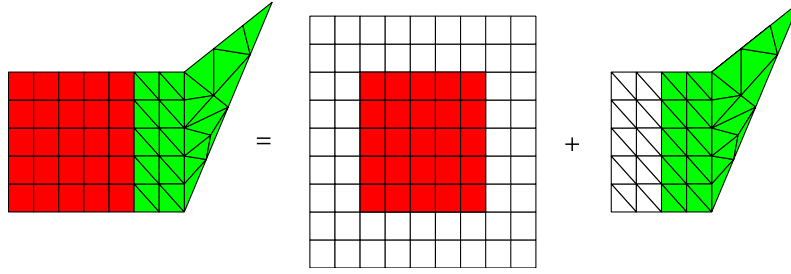


Fig. 3. Principle of the division into patches of structured and unstructured grids with $n_{\text{ghost}} = 2$. White cells are ghost cells, which are updated either by the boundary conditions or due to mappings in between the patches.

3.2. Hybrid grid generation in two dimensions

The idea of the two-dimensional method follows the same idea, i.e., we split the domain into structured and unstructured parts, see Fig. 3. At each time step, we update the ghost cells to connect the different patches. In the structured parts we use a standard two-dimensional WENO method and in the unstructured parts we apply the RBF-ENO method. Next, we update the missing left or right reconstruction values at each interface. Note that the standard WENO method is based on ghost cells on each side, but the RBF-ENO method is not, see Remark 2.1. Let us define $\Omega \in \mathbb{R}^2$ as the interior of the computational domain such that the ghost cells from the WENO method at the boundary are outside of Ω . As for the one-dimensional version, we add n_{ghost} squares from the structured to the unstructured part, but we triangulate them artificially, e.g., the green structured triangulation in Fig. 3. To ensure the connection between the domains we create the ghost cells for the green structured triangulation and define a map between the ghost cells of the triangular side and the overlapping quadrilaterals of the structured grid and vice versa. We have the following two kinds of ghost cells

- ghost cells that connect two different patches (they overlap with interior cells of other patches);
- ghost cells that are outside of the boundary to apply the structured WENO method (they are always quadrilaterals).

We define the three maps

$$f_{\text{TRI}} : \text{GHOST}_{\text{TRI}} \rightarrow \text{INTERNAL}, \tag{36}$$

$$f_{\text{QUAD},1} : \text{GHOST}_{\text{QUAD}} \rightarrow \text{INTERNAL}, \tag{37}$$

$$f_{\text{QUAD},2} : \text{GHOST}_{\text{QUAD}} \rightarrow \text{INTERNAL}, \tag{38}$$

to set the value for each ghost cell. These maps have the following properties

- For each $T \in \text{GHOST}_{\text{TRI}}$ there exists one $\tilde{T} \in \text{GHOST}_{\text{TRI}}$ such that $f_{\text{TRI}}(T) = f_{\text{TRI}}(\tilde{T})$ and $T \neq \tilde{T}$. Furthermore, it holds $T, \tilde{T} \subset f_{\text{TRI}}(T)$;
- For each $Q \in \text{GHOST}_{\text{QUAD}}$ with $Q \subset \Omega$ there exist $T, \tilde{T} \in \text{INTERNAL}_{\text{TRI}}$ or $\tilde{Q} \in \text{INTERNAL}_{\text{QUAD}}$ with $T \neq \tilde{T}$ such that $f_{\text{QUAD},1}(Q) = T$ and $f_{\text{QUAD},2}(Q) = \tilde{T}$ or $f_{\text{QUAD},1}(Q) = f_{\text{QUAD},2}(Q) = \tilde{Q}$. Again, we have the condition $T, \tilde{T}, \tilde{Q} \subset Q$;
- For each $Q \in \text{GHOST}_{\text{QUAD}}$ with $Q \not\subset \Omega$, there exists $\tilde{Q} \in \text{INTERNAL}_{\text{QUAD}}$ such that $f_{\text{QUAD},1}(Q) = f_{\text{QUAD},2}(Q) = \tilde{Q}$.

Instead of the update (32) and (33) we use the average of the two overlapping triangles with the quadrilateral ghost cell (in case of a QUAD to QUAD map $f_{\text{QUAD},1}(Q) = f_{\text{QUAD},2}(Q)$)

$$U_T = U_{f_{\text{TRI}}(T)}, \quad \text{for each } T \in \text{GHOST}_{\text{TRI}}, \tag{39}$$

$$U_Q = \frac{U_{f_{\text{QUAD},1}(Q)} + U_{f_{\text{QUAD},2}(Q)}}{2}, \quad \text{for each } Q \in \text{GHOST}_{\text{QUAD}}. \tag{40}$$

The functions (34) and (35) can be defined in the same way as before, since every edge has a unique direction which defines a right and a left cell for each edge. To define the different patches and maps for hybrid grids in multiple dimensions, we need to introduce some additional tools. Let us defined the following kind of patches

- quadrilaterals (QUAD);
- connection patches between two QUADs (Q2Q);
- connection patches between multiple Q2Qs (RQ);
- the triangular patches (TRI).

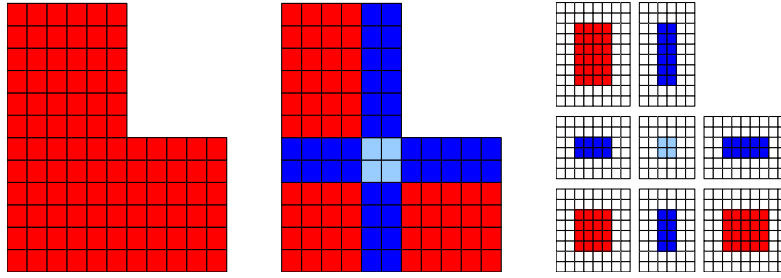


Fig. 4. Principle of the division into patches of just structured grids for an L-shaped domain with $n_{ghost} = 2$. White cells are ghost cells, which are updated either by the boundary conditions or due to mappings between the patches.

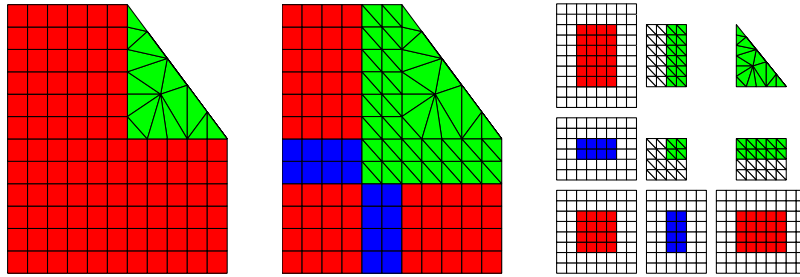


Fig. 5. Principle of the division into patches of structured and unstructured grids with $n_{ghost} = 2$. White cells are ghost cells, which are updated either by the boundary conditions or due to mappings between the patches.

To automate the generation of the ghost cells we divide the TRI patches into

- the principle triangular part (TRIO);
- the connection patches between TRI0s and QUADs (Q2T);
- the small connection patches that connect all kind of combinations of Q2Ts and Q2Qs in the case of at least one Q2T (RT).

Fig. 4 illustrates a way to combine quadrilateral grids. The L-shaped domain is divided into three QUADs, four Q2Qs, and one RQ patches. Note that we can use Q2Q-patches also at the boundary. The only restriction is that the grid size in each direction is uniform and we require that each side length is a multiple of its grid size.

Let us take a look at Fig. 5 to illustrate how to combine the pieces in case we also have triangular parts. We have a single TRI0, two Q2T, one RT, two Q2Q and three QUAD patches. The only unstructured patches are the TRI0s. The Q2T's are long patches of width $n_{ghost}\Delta x$ or $n_{ghost}\Delta y$ with a structured triangulation and ghost cells only in one direction. The RTs are of size $n_{ghost}\Delta x \times n_{ghost}\Delta y$ with a structured triangulation and its ghost cells are added just in the direction of Q2Q patches and over the corners in between two Q2Q patches.

Given the tools described above we can construct hybrid grids for general geometries. This hybrid method can be used to locally refine grids and apply a fast structured solver around this refined region. Fig. 6 shows a possible local refinement with a central unstructured domain.

3.3. Setting of the WENO and RBF-ENO methods

In the following, we describe the specific setting of the RBF-ENO and WENO methods, used on the hybrid grids.

3.3.1. One-dimensional hybrid method

On the structured patches we use the standard WENO method of order p_{WENO} and on the unstructured patches we use the RBF-ENO method of order p_{ENO} . Let us consider the one-dimensional RBF-ENO method, introduced in Section 2.3. To construct a method of order p the choice of $p_{ENO} = p$ is given. For the WENO method there are two possibilities

$$p_{WENO} = 2 \left\lfloor \frac{p}{2} \right\rfloor + 1, \quad \text{with the stencil size } n = 2 \left\lfloor \frac{p}{2} \right\rfloor + 1, \quad (41)$$

$$p_{WENO} = 2p - 1, \quad \text{with the stencil size } n = 2p - 1, \quad (42)$$

with different orders of convergence. The following theorem states the stability result.

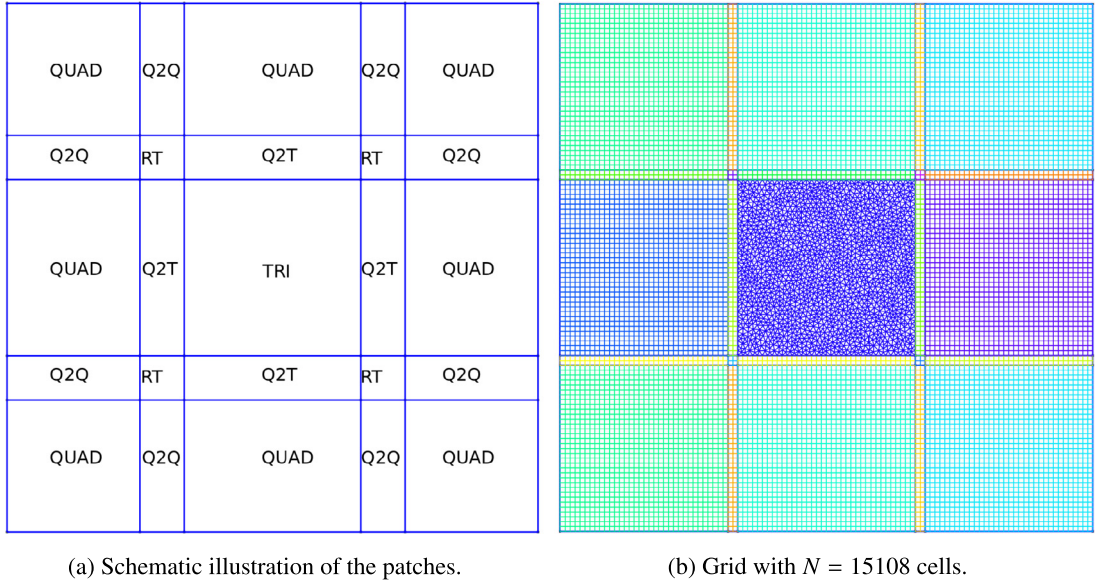


Fig. 6. Hybrid grid with a central unstructured part.

Theorem 3.1 (Stability and order of convergence). Given the hybrid RBF-ENO method with $p_{\text{ENO}} = p$ and

$$p_{\text{WENO}} = 2 \left\lfloor \frac{p}{2} \right\rfloor + 1, \tag{43}$$

or

$$p_{\text{WENO}} = 2p - 1. \tag{44}$$

It provides an accuracy of order p for smooth solutions. Furthermore, the combination of the two methods is stable if both methods are stable. Thus, Δt must be the smallest time step fulfilling the CFL-condition over all patches and the number of ghost cells $n_{\text{ghost}} \geq p - 1$ such that both methods are stable.

Proof. Given the RBF-ENO method of order $p_{\text{ENO}} = p$, the WENO method of order p_{WENO} by (41) or (42) and the number of ghost cells $n_{\text{ghost}} = p - 1$, we get that in the smooth case each part of the method has an accuracy of order p . Thus, each flux is of order $p - 1$. Since $n_{\text{ghost}} \geq p - 1$ the reconstruction of both the RBF-ENO and the WENO method is locally the same as for each individual reconstruction. In the end, for Δt the smallest time step fulfilling the CFL-condition, we get the same stability as for each method itself. \square

There are no general stability results for the WENO and ENO method. The stability we conjecture states that the hybrid method is as stable as the single methods and the combination of the two does not destroy this.

3.3.2. Two-dimensional hybrid method of order three

In two space dimensions, we restrict ourselves to the case $p_{\text{ENO}} = 3$ on the unstructured patches. Since the two-dimensional WENO method is based on dimensional splitting we have the conditions (41) or (42) on the structured patches. We use the standard WENO method of order $p_{\text{WENO}} = 5$ since the computational cost is similar. To receive $p_{\text{WENO}} = 5$ in the smooth case we need

$$p_{\text{WENO}} \leq 2n_{\text{ghost}} + 1. \tag{45}$$

Furthermore, we need the number of ghost cells n_{ghost} to be large enough such that the RBF-ENO method is flexible enough to avoid oscillatory states. This results in the result of Theorem 3.1.

Theorem 3.2 (Stability). The high-order hybrid RBF-ENO method is stable with respect to the smallest time step Δt over all patches if the number of ghost cells n_{ghost} is large enough such that (45) is fulfilled and such that all neighbors until d_{max} are inside the ghost cell area.

Proof. To have no restrictions for the RBF-ENO method, we need to choose n_{ghost} such that all neighbors until d_{max} , the maximal distance introduced in Table 2, are inside the ghost cell patches. For the WENO method we require (45). To get the

5	5	5	
	4	4	
5	3	3	
	4	2	
5	3	1	0
	4	2	
	5	3	
		4	
			5

Fig. 7. Number of ghost cells n_{ghost} needed for the RBF-ENO method depending on d_{max} from Table 2.

same stability as for each single method, it remains to satisfy the CFL condition for Δt on each patch of the computational domain. \square

Remark 3.2. In one dimension, this method is high-order accurate. However, if we implement the WENO method in two-dimensions with the standard flux splitting we recover only a high-resolution method. There is a way of evaluating the WENO reconstruction on each edge at some high-order quadrature nodes, but this is costly. Another possibility is the accuracy correction proposed by Buchmüller and Helzel [29].

For the RBF-ENO method of order 3 we have $d_{\text{max}} = 5$. Thus, with $n_{\text{ghost}} = 3$ all neighbors can be considered, see Fig. 7. However, except for the final example of the flow through a conical aerospike nozzle, we choose $n_{\text{ghost}} = 2$. In the last example, we must choose $n_{\text{ghost}} = 3$ to avoid negative pressure.

4. Maximum preserving limiter

In this section, we show that the maximum preserving principle introduced by Perthame and Shu [23] and Zhang and Shu [30] can be generalized to non-polynomial reconstructions. Hence, we can apply it for the triangular part of the hybrid high-resolution RBF-ENO method. The structured part can be stabilized using the positivity preserving limiter for the WENO method in each direction [30].

4.1. Generalized maximum preserving limiter

The maximum principle satisfying finite volume method is based on the first order finite volume scheme (8)

$$U_i^{n+1} = U_i^n - \lambda[F(U_i^n, U_{i+1}^n) - F(U_{i-1}^n, U_i^n)] =: H_\lambda(U_{i-1}^n, U_i^n, U_{i+1}^n), \quad (46)$$

with a monotone numerical flux F and $\lambda = \Delta t/\Delta x$. For suitable numerical flux functions, e.g., the monotone Rusanov and Godunov schemes, H_λ is increasing in each argument under the CFL condition $\max_u |\nabla_u f(u)|\lambda \leq 1$. Using the consistency of the flux we have the maximum principle

$$m = H_\lambda(m, m, m) \leq U_i^{n+1} = H_\lambda(U_{i-1}^n, U_i^n, U_{i+1}^n) \leq H_\lambda(M, M, M) = M, \quad (47)$$

for $m \leq U_{i-1}^n, U_i^n, U_{i+1}^n \leq M$. Let us consider the high-order MUSCL scheme

$$U_i^{n+1} = U_i^n - \lambda[F(u_{i+1/2}^-, u_{i+1/2}^+) - F(u_{i-1/2}^-, u_{i-1/2}^+)], \quad (48)$$

with $u_{i-1/2}^+ = p_i(x_{i-1/2})$ and $u_{i+1/2}^- = p_i(x_{i+1/2})$ of the high-order polynomial $p_i \in \Pi^k(\mathbb{R})$ interpolating on a stencil around the cell i . Note, it is enough to show the idea for the forward Euler method in time since the MUSCL scheme with a SSPRK method can be written as convex combinations of (48). The idea is to express the average value of each cell by the exact Gauss-Lobatto quadrature rule with nodes $\hat{x}_i^\alpha \in [x_{i-1/2}, x_{i+1/2}]$ and the weights $\hat{\omega}_\alpha$ for $\alpha = 1, \dots, N$ with $2N - 3 \geq k$, i.e.,

$$U_i^n = \sum_{\alpha=1}^N \hat{\omega}_\alpha p_i(\hat{x}_i^\alpha), \quad (49)$$

with $\hat{x}_i^1 = x_{i-1/2}$ and $\hat{x}_i^N = x_{i+1/2}$. The maximum preserving limiter is based on the following form of (48)

$$U_i^{n+1} = \sum_{\alpha=2}^{N-1} \hat{\omega}_\alpha p_i(\hat{x}_i^\alpha) + \hat{\omega}_N \left(u_{i+1/2}^- - \frac{\lambda}{\hat{\omega}_N} [F(u_{i+1/2}^-, u_{i+1/2}^+) - F(u_{i-1/2}^+, u_{i+1/2}^-)] \right) + \hat{\omega}_1 \left(u_{i-1/2}^+ - \frac{\lambda}{\hat{\omega}_1} [F(u_{i-1/2}^+, u_{i+1/2}^-) - F(u_{i-1/2}^-, u_{i-1/2}^+)] \right), \quad (50)$$

where we added and subtracted $F(u_{i-1/2}^+, u_{i+1/2}^-)$. This can be expressed as

$$U_i^{n+1} = \sum_{\alpha=2}^{N-1} \hat{\omega}_\alpha p_i(\hat{x}_i^\alpha) + \hat{\omega}_N H_{\lambda/\hat{\omega}_N}(p_i(\hat{x}_i^1), p_i(\hat{x}_i^N), p_{i+1}(\hat{x}_{i+1}^1)) + \hat{\omega}_1 H_{\lambda/\hat{\omega}_1}(p_{i-1}(\hat{x}_{i-1}^N), p_i(\hat{x}_i^1), p_i(\hat{x}_i^N)). \quad (51)$$

Under the CFL condition

$$\lambda \max_u |\nabla_u f(u)| \leq \min_\alpha \hat{\omega}_\alpha, \quad (52)$$

and

$$m \leq p_j(\hat{x}_j^\alpha) \leq M, \quad \text{for all } \alpha = 1, \dots, N, \quad \text{and } j = i-1, i, j+1, \quad (53)$$

we ensure the satisfaction of the maximum principle $m \leq U_i^{n+1} \leq M$. However, we can rewrite the method in a slightly different form

$$U_i^{n+1} = \hat{\omega}_R p_R + \hat{\omega}_N H_{\lambda/\hat{\omega}_N}(u_{i-1/2}^+, u_{i+1/2}^-, u_{i+1/2}^+) + \hat{\omega}_1 H_{\lambda/\hat{\omega}_1}(u_{i-1/2}^-, u_{i-1/2}^+, u_{i+1/2}^-), \quad (54)$$

with $\hat{\omega}_R = 1 - \hat{\omega}_N - \hat{\omega}_1 \geq 0$ and

$$p_R = \sum_{\alpha=2}^{N-1} \frac{\hat{\omega}_\alpha}{\hat{\omega}_R} p(\hat{x}_i^\alpha) = \frac{U_i^n - \hat{\omega}_N u_{i+1/2}^- - \hat{\omega}_1 u_{i-1/2}^+}{\hat{\omega}_R}. \quad (55)$$

Again, we satisfy the maximum principle $m \leq U_i^{n+1} \leq M$ under the milder condition

$$m \leq p_R, u_{j+1/2}^-, u_{j-1/2}^+ \leq M, \quad \text{for } j = i-1, i, i+1. \quad (56)$$

Based on these results we define the limiter

$$\tilde{p}(x) = \tilde{\theta}(p(x) - U_i^n) + U_i^n, \quad (57)$$

$$\tilde{\theta} = \min \left\{ \left| \frac{U_i^n - m}{U_i^n - \tilde{u}_{\min}} \right|, \left| \frac{U_i^n - M}{U_i^n - \tilde{u}_{\max}} \right|, 1 \right\}, \quad (58)$$

$$\tilde{u}_{\min} = \min\{p_R, u_{i+1/2}^-, u_{i-1/2}^+\}, \quad \tilde{u}_{\max} = \max\{p_R, u_{i-1/2}^-, u_{i+1/2}^+\}. \quad (59)$$

The original limiter from Zhang and Shu [30] is

$$\hat{p}(x) = \theta(p(x) - U_i^n) + U_i^n, \quad \theta = \min \left\{ \left| \frac{U_i^n - m}{U_i^n - u_{\min}} \right|, \left| \frac{U_i^n - M}{U_i^n - u_{\max}} \right|, 1 \right\}, \quad (60)$$

$$u_{\min} = \min_\alpha p(\hat{x}_i^\alpha), \quad u_{\max} = \max_\alpha p(\hat{x}_i^\alpha). \quad (61)$$

Lemma 4.1 verifies that the new limiter is conservative, maintains accuracy and

$$U_i^{n+1} = \hat{\omega}_R \tilde{p}_R + \hat{\omega}_N H_{\lambda/\hat{\omega}_N}(\tilde{p}_i(\hat{x}_i^1), \tilde{p}_i(\hat{x}_i^N), \tilde{p}_{i+1}(\hat{x}_{i+1}^1)) + \hat{\omega}_1 H_{\lambda/\hat{\omega}_1}(\tilde{p}_{i-1}(\hat{x}_{i-1}^N), \tilde{p}_i(\hat{x}_i^1), \tilde{p}_i(\hat{x}_i^N)), \quad (62)$$

with

$$\tilde{p}_R := \frac{U_i^n - \hat{\omega}_1 \tilde{p}(\hat{x}_i^1) - \hat{\omega}_N \tilde{p}(\hat{x}_i^N)}{\hat{\omega}_R}, \quad (63)$$

satisfies the maximum condition.

Lemma 4.1. *The simplified maximum preserving limiter (57) with (58) and (59) is conservative, of high order, and satisfies the maximum condition (56).*

Proof. Conservation: Conservation is clear as p is conserved

$$\frac{1}{|C|} \int_C \tilde{p}(x) dx = \frac{\tilde{\theta}}{|C|} \int_C p(x) dx + (1 - \tilde{\theta}) U_i^n = U_i^n. \quad (64)$$

Accuracy: Let us assume the case $\tilde{\theta} = \left| \frac{U_i^n - m}{U_i^n - \tilde{u}_{\min}} \right|$. The other case works in the same manner. From Zhang and Shu [31] we have

$$|\hat{p}(x) - p(x)| = \mathcal{O}(\Delta x^{k+1}). \quad (65)$$

Furthermore, we know

$$u_{\min} \leq \tilde{u}_{\min}, \quad (66)$$

since $u_{i-1/2}^+ = p(\hat{x}_1)$, $u_{i+1/2}^- = p(\hat{x}_N)$ and p_R is a convex combination of values $p(\hat{x}_i^\alpha)$. If we assume $\tilde{\theta} < 1$ we obtain $u_{\min} \leq \tilde{u}_{\min} < m$ and $\theta \leq \tilde{\theta} \leq 1$. Using the definition of the limiter and combining it with the previous results, we have

$$|\hat{p}(x) - p(x)| = |\theta(p(x) - U_i^n) + U_i^n - p(x)| = |\theta - 1||p(x) - U_i^n| \geq |\tilde{\theta} - 1||p(x) - U_i^n| = |\tilde{p}(x) - p(x)|. \quad (67)$$

With (65) we conclude

$$|\tilde{p}(x) - p(x)| = \mathcal{O}(\Delta x^{k+1}). \quad (68)$$

Maximum preserving condition: By construction we have $m \leq \tilde{p}(x_{i-1/2})$, $\tilde{p}(x_{i+1/2}) \leq M$. Further, we have

$$\begin{aligned} \tilde{p}_R &= \frac{U_i^n - \hat{\omega}_1 \tilde{p}(\hat{x}_1^1) - \hat{\omega}_N \tilde{p}(\hat{x}_i^N)}{\hat{\omega}_R} = \frac{\tilde{\theta} U_i^n + (1 - \tilde{\theta}) U_i^n + \hat{\omega}_1 (\tilde{\theta} - 1) U_i^n - \hat{\omega}_1 \tilde{\theta} p(\hat{x}_1^1) + \hat{\omega}_N (\tilde{\theta} - 1) U_i^n - \hat{\omega}_N \tilde{\theta} p(\hat{x}_i^N)}{\hat{\omega}_R}, \\ &= \tilde{\theta} p_R + (1 - \tilde{\theta}) U_i^n. \end{aligned}$$

Thus, we have $m \leq \tilde{p}_R \leq M$. \square

4.2. WENO limiter

The challenge with the standard WENO method compared to the ENO method is that we do not recover the high-order interpolation function, but just the values $u_{i\pm 1/2}^\pm$. Zhang and Shu [30] introduced a way to resolve this issue by reconstructing $p \in \Pi^k(\mathbb{R})$ using $u_{i-1/2}^+$, $u_{i+1/2}^-$ and surrounding cell averages U_j for $j = i - k_0, \dots, i + k_1$ for $k_0, k_1 \in \mathbb{N}$. Given the idea from the previous section, we can create a limiter by using the extrema preserving limiter (57) without artificially generating a reconstruction $p \in \Pi^k(\mathbb{R})$. For the two-dimensional WENO method on structured grids, based on dimensional splitting [26], we apply the one-dimensional maximum preserving limiter in each dimension [30].

4.3. Non-polynomial reconstruction

In the case of a non-polynomial reconstruction, condition (49) is not satisfied. However, we can make use of the concept behind (55). Let us consider the reconstruction $r : \mathbb{R} \rightarrow \mathbb{R}$ of order k . We define

$$p_R = \frac{U_i^n - \hat{\omega}_N u_{i+1/2}^- - \hat{\omega}_1 u_{i-1/2}^+}{\hat{\omega}_R}, \quad (69)$$

with the Gauss-Lobatto weights $\hat{\omega}_1, \hat{\omega}_N > 0$, $N \in \mathbb{N}$ such that $2N - 3 \geq k$ and

$$\hat{\omega}_R = 1 - \hat{\omega}_1 - \hat{\omega}_N. \quad (70)$$

As before, we can rewrite U_i^{n+1} using (54). The scheme is extrema preserving if (56) is fulfilled. If it is not fulfilled, we use $\tilde{\theta}$ from (58) and define the limiter

$$\tilde{r}(x) = \tilde{\theta}(r(x) - U_i^n) + U_i^n. \quad (71)$$

As in the polynomial case, this limiter defines a high-order, conservative reconstruction fulfilling the extrema-preserving condition (56), see Lemma 4.2. Finally, we define the extrema-preserving MUSCL scheme with non-polynomial reconstruction

$$U^{n+1} = U^n - \lambda[F(\tilde{r}_i(x_{i+1/2}), \tilde{r}_{i+1}(x_{i+1/2})) - F(\tilde{r}_{i-1}(x_{i-1/2}), \tilde{r}_i(x_{i-1/2}))]. \quad (72)$$

Lemma 4.2. *The simplified positivity preserving limiter (71) is conservative, of high order, and satisfies the simplified maximum preserving condition (56).*

Proof. The proof for the consistency and the maximum preserving property follows Lemma 4.1. To show high-order accuracy, we introduce the polynomial $p \in \Pi^k(\mathbb{R})$ which interpolates the reconstructed values $r(\hat{x}_i^\alpha)$ at the points \hat{x}_i^α for $\alpha = 1, \dots, N$ with the property

$$|r(x) - p(x)| = \mathcal{O}(\Delta x^{k+1}). \quad (93)$$

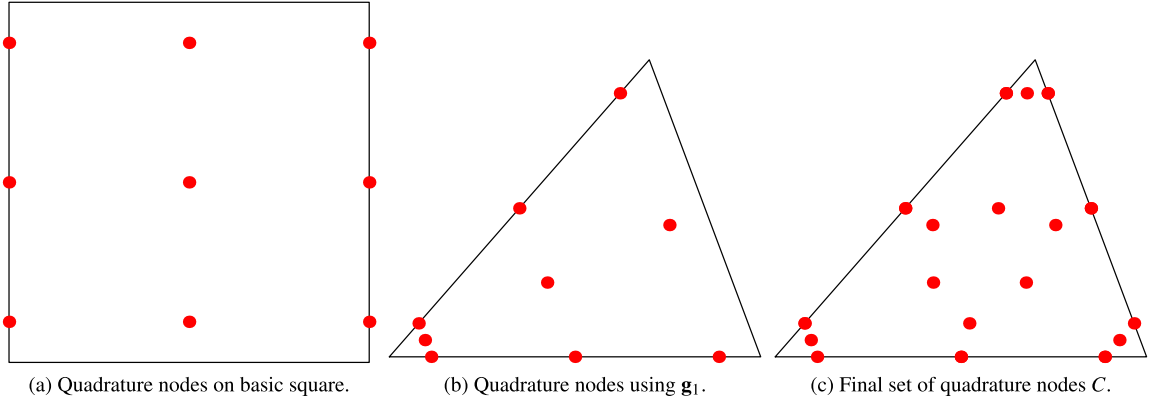


Fig. 8. Construction of quadrature nodes for $k = 2$.

Further, we define the maximum preserving limiter \tilde{p} based on (58). Since r and p have the same values on the quadrature nodes, the scaling parameters $\tilde{\theta}_p$ and $\tilde{\theta}_r$ coincide. We expand the difference between the limited and the original reconstruction

$$|\tilde{r}(x) - r(x)| \leq |\tilde{r}(x) - \tilde{p}(x)| + |\tilde{p}(x) - p(x)| + |p(x) - r(x)|. \tag{74}$$

By construction, we have $|p(x) - r(x)| = \mathcal{O}(\Delta x^{k+1})$ and from Lemma 4.1 we know $|\tilde{p}(x) - p(x)| = \mathcal{O}(\Delta x^{k+1})$. Since the scaling parameter $\tilde{\theta}_r, \tilde{\theta}_p$ coincides, we have

$$|\tilde{r}(x) - \tilde{p}(x)| = \tilde{\theta}_r |r(x) - p(x)| = \mathcal{O}(\Delta x^{k+1}), \tag{75}$$

and conclude that $|\tilde{r}(x) - r(x)| = \mathcal{O}(\Delta x^{k+1})$. \square

4.4. General reconstruction on triangular grids

Zhang et al. [32] introduced a generalization of the maximum preserving limiter to triangular elements. Here, we change the method to define it for non-polynomial reconstructions. The idea is to define a quadrature rule on the triangle of the right order such that the weights are positive and all Gauss quadrature points on the interface are included. This quadrature rule is based on quadrature points on the square $[-\frac{1}{2}, \frac{1}{2}] \times [-\frac{1}{2}, \frac{1}{2}]$ defined as the product of the $k + 1$ Gauss quadrature points $\{\hat{u}^\beta | \beta = 1, \dots, k + 1\}$ with its weights ω_β and the N Gauss-Lobatto quadrature points $\{\hat{u}^\alpha | \alpha = 1, \dots, N\}$ with its weights $\hat{\omega}_\alpha$ and $2N - 3 \geq k$. Thus, we have the quadrature points

$$S_k = \{(\hat{u}^\alpha, v^\beta) | \alpha = 1, \dots, k + 1, \beta = 1, \dots, N\}, \tag{76}$$

with the quadrature weights $\omega_\beta \hat{\omega}_\alpha$ on the square $[-\frac{1}{2}, \frac{1}{2}] \times [-\frac{1}{2}, \frac{1}{2}]$. Given the triangle C with the vertices $\mathbf{V}_1, \mathbf{V}_2, \mathbf{V}_3$ oriented clockwise, we define

$$\mathbf{g}_1(u, v) = \left(\frac{1}{2} + v\right)\mathbf{V}_1 + \left(\frac{1}{2} + u\right)\left(\frac{1}{2} - v\right)\mathbf{V}_2 + \left(\frac{1}{2} - u\right)\left(\frac{1}{2} - v\right)\mathbf{V}_3, \tag{77}$$

$$\mathbf{g}_2(u, v) = \left(\frac{1}{2} + v\right)\mathbf{V}_2 + \left(\frac{1}{2} + u\right)\left(\frac{1}{2} - v\right)\mathbf{V}_3 + \left(\frac{1}{2} - u\right)\left(\frac{1}{2} - v\right)\mathbf{V}_1, \tag{78}$$

$$\mathbf{g}_3(u, v) = \left(\frac{1}{2} + v\right)\mathbf{V}_3 + \left(\frac{1}{2} + u\right)\left(\frac{1}{2} - v\right)\mathbf{V}_1 + \left(\frac{1}{2} - u\right)\left(\frac{1}{2} - v\right)\mathbf{V}_2, \tag{79}$$

from the square to the triangle C . These map the top edge of the square to one vertex of the triangle, see Fig. 8(b). The following Lemma gives us the determinants of the gradient of the projections.

Lemma 4.3 (Jacobian of the projections [32]). *If the orientation of the three vertices $\mathbf{V}_1, \mathbf{V}_2$ and \mathbf{V}_3 is clockwise, then the Jacobian $|\nabla \mathbf{g}_{l_e}(u, v)| = 2|C|(\frac{1}{2} - v)$ for $l_e = 1, 2, 3$.*

Given the three different projections, we define the set of new quadrature nodes

$$S_k^C = \mathbf{g}_1(S_k) \cup \mathbf{g}_2(S_k) \cup \mathbf{g}_3(S_k), \tag{80}$$

which include all Gauss points on the cell boundary, e.g., see Fig. 8(c) for the case $k = 2$. Now, we can rewrite the cell average

$$U_C^n = \frac{1}{|C|} \int_C p_C(\mathbf{x}) d\mathbf{x} = \frac{1}{|C|} \int_{-1/2}^{1/2} \int_{-1/2}^{1/2} p_C(\mathbf{g}_{l_e}(u, v)) |\nabla \mathbf{g}_{l_e}(u, v)| dudv, \tag{81}$$

for $p_C \in \Pi^k(\mathbb{R}^2)$ and $i = 1, 2, 3$. Thus, we can take the average over all $i = 1, 2, 3$

$$U_C^n = \frac{1}{3|C|} \sum_{l_e=1}^3 \int_{-1/2}^{1/2} \int_{-1/2}^{1/2} p_C(\mathbf{g}_{l_e}(u, v)) |\nabla \mathbf{g}_{l_e}(u, v)| dudv, \tag{82}$$

$$= \sum_{l_e=1}^3 \sum_{\alpha=1}^N \sum_{\beta=1}^{k+1} p_C(\mathbf{g}_{l_e}(\hat{u}^\alpha, v^\beta)) \frac{2}{3} \left(\frac{1}{2} - v^\beta\right) \omega_\alpha \hat{\omega}_\beta = \sum_{\mathbf{x} \in S_k^C} p_C(\mathbf{x}) \omega_{\mathbf{x}}, \tag{83}$$

using the result of Lemma 4.3 with the quadrature weights $\omega_{\mathbf{x}}$ for each $\mathbf{x} \in S_k^C$. We define the set of quadrature points in the interior $S_k^{C,int}$ and the set of quadrature points on the edges $S_k^{C,edg}$. Note that in (83) each quadrature node on the edge is counted double with $\hat{\omega}_1 = \hat{\omega}_N$. We obtain

$$S_k^{C,edg} = \left\{ \mathbf{x}_{1,\beta}, \mathbf{x}_{2,\beta}, \mathbf{x}_{3,\beta} \mid \beta = 1, \dots, k+1 \right\}, \tag{84}$$

with $\mathbf{x}_{1,\beta} = (0, \frac{1}{2} + v^\beta, \frac{1}{2} - v^\beta)$, $\mathbf{x}_{2,\beta} = (\frac{1}{2} - v^\beta, 0, \frac{1}{2} + v^\beta)$, $\mathbf{x}_{3,\beta} = (\frac{1}{2} + v^\beta, \frac{1}{2} - v^\beta, 0)$ written in terms of the barycentric coordinates (ξ_1, ξ_2, ξ_3) , such that $\mathbf{p} = \xi_1 \mathbf{V}_1 + \xi_2 \mathbf{V}_2 + \xi_3 \mathbf{V}_3$. To calculate the weights on the edge $(0, \frac{1}{2} + v^\beta, \frac{1}{2} - v^\beta)$ we use that $\mathbf{g}_2(\frac{1}{2}, v^\beta) = \mathbf{g}_3(-\frac{1}{2}, -v^\beta)$ and recover

$$\frac{2}{3} \left(\frac{1}{2} + v^\beta\right) \omega_\beta \hat{\omega}_1 + \frac{2}{3} \left(\frac{1}{2} - v^\beta\right) \omega_\beta \hat{\omega}_N = \frac{2}{3} \omega_\beta \hat{\omega}_1, \tag{85}$$

for the weights on the edges for the quadrature node $\mathbf{x}_{1,\beta}$. The same result is obtained for the other edges. Analogous to the one-dimensional case, we have

$$U_C^n = p_R \omega_R + \sum_{\beta=1}^{k+1} \sum_{l_e=1}^3 \frac{2}{3} \omega_\beta \hat{\omega}_1 u_{l_e,\beta}^C, \tag{86}$$

with the evaluation of the quadrature node on the l_e th edge $u_{l_e,\beta}^C = p_C(\mathbf{x}_{l_e,\beta})$,

$$\omega_R = 1 - \sum_{\beta=1}^{k+1} \sum_{l_e=1}^3 \frac{2}{3} \omega_\beta \hat{\omega}_1, \quad \text{and} \quad p_R = \sum_{\mathbf{x} \in S_k^{C,int}} p_C(\mathbf{x}) \frac{\omega_{\mathbf{x}}}{\omega_R} = \frac{U_C}{\omega_R} - \sum_{\beta=1}^{k+1} \sum_{l_e=1}^3 \frac{2}{3} \frac{\omega_\beta \hat{\omega}_1}{\omega_R} u_{l_e,\beta}^C. \tag{87}$$

Let us rewrite the finite volume scheme (4) with the high order flux (11) and the forward Euler method in time, i.e.,

$$U_i^{n+1} = U_i^n - \frac{\Delta t}{|C_i|} \sum_{\beta=1}^{k+1} \omega_\beta \sum_{l_e=1}^3 F_{il_e}(u_{l_e,\beta}^{C_i}, u_{l_e,\beta}^{C_{il_e}}, \mathbf{n}_{il_e}). \tag{88}$$

The proof of the maximum principle is based on the requirement that the first order method

$$U_i^{n+1} = U_i^n - \lambda \sum_{l_e=1}^3 F_{il_e}(U_i^n, U_{il_e}^n, \mathbf{n}_{il_e}), \tag{89}$$

is non-decreasing under the CFL condition

$$\max_{u, \mathbf{n}} |\nabla_u(f(u) \cdot \mathbf{n})| \lambda \sum_{l_e=1}^3 |S_{il_e}| \leq 1, \tag{90}$$

which is satisfied for a monotone flux, e.g., the Rusanov flux (6).

Theorem 4.4 (Maximum principle satisfying scheme for triangular grids). *Let us consider a first order finite volume method of the form (89) that is non-decreasing under the condition (90). The scheme (88) satisfies the maximum principle*

$$m \leq U_{C_i}^{n+1} \leq M, \tag{91}$$

under the condition that

$$m \leq u_{l_e, \beta}^{C_i}, p_R \leq M, \quad \text{for all } l_e = 1, 2, 3, \beta = 1, \dots, k + 1, \quad (92)$$

and the additional CFL condition

$$\max_{u, \mathbf{n}} |\nabla_u(f(u) \cdot \mathbf{n})| \frac{\Delta t}{|C_i|} \sum_{l_e=1}^3 |S_{il_e}| \leq \frac{2}{3} \hat{\omega}_1, \quad (93)$$

Proof. The proof follows the one in [32] with the difference that we use p_R defined in (87). Let us decompose the flux (88)

$$\begin{aligned} \sum_{l_e=1}^3 F_{il_e}(u_{i, \beta}^{C_i}, u_{i, \beta}^{C_{l_e}}, \mathbf{n}_{il_e}) &= F_{i1}(u_{1, \beta}^{C_i}, u_{1, \beta}^{C_{i1}}, \mathbf{n}_{i1}) + F_{i1}(u_{1, \beta}^{C_i}, u_{2, \beta}^{C_i}, -\mathbf{n}_{i1}) + F_{i1}(u_{2, \beta}^{C_i}, u_{1, \beta}^{C_i}, \mathbf{n}_{i1}) \\ &+ F_{i2}(u_{2, \beta}^{C_i}, u_{2, \beta}^{C_{i2}}, \mathbf{n}_{i2}) + F_{i3}(u_{2, \beta}^{C_i}, u_{3, \beta}^{C_i}, \mathbf{n}_{i3}) + F_{i3}(u_{3, \beta}^{C_i}, u_{2, \beta}^{C_i}, -\mathbf{n}_{i3}) + F_{i3}(u_{3, \beta}^{C_i}, u_{3, \beta}^{C_{i3}}, \mathbf{n}_{i3}), \end{aligned} \quad (94)$$

by the conservation of the flux. Next, we combine (88) with (86) and (94) and obtain

$$\begin{aligned} U_i^{n+1} &= p_R \omega_R + \sum_{\beta=1}^{k+1} \sum_{l_e=1}^3 \frac{2}{3} \omega_\beta \hat{\omega}_1 u_{l_e, \beta}^{C_i} - \frac{\Delta t}{|C_i|} \sum_{\beta=1}^{k+1} \omega_\beta \sum_{l_e=1}^3 F_{il_e}(u_{l_e, \beta}^{C_i}, u_{l_e, \beta}^{C_{l_e}}, \mathbf{n}_{il_e}) \\ &= p_R \omega_R + \sum_{\beta=1}^{k+1} \frac{2}{3} \omega_\beta \hat{\omega}_1 [H_{1, \beta} + H_{2, \beta} + H_{3, \beta}], \end{aligned}$$

with

$$\begin{aligned} H_{1, \beta} &= u_{1, \beta}^{C_i} - \frac{3\Delta t}{2\hat{\omega}_1 |C_i|} [F_{i1}(u_{1, \beta}^{C_i}, u_{1, \beta}^{C_{i1}}, \mathbf{n}_{i1}) + F_{i1}(u_{1, \beta}^{C_i}, u_{2, \beta}^{C_i}, -\mathbf{n}_{i1})], \\ H_{2, \beta} &= u_{2, \beta}^{C_i} - \frac{3\Delta t}{2\hat{\omega}_1 |C_i|} [F_{i1}(u_{2, \beta}^{C_i}, u_{1, \beta}^{C_i}, \mathbf{n}_{i1}) + F_{i2}(u_{2, \beta}^{C_i}, u_{2, \beta}^{C_{i2}}, \mathbf{n}_{i2}) + F_{i3}(u_{2, \beta}^{C_i}, u_{3, \beta}^{C_i}, \mathbf{n}_{i3})], \\ H_{3, \beta} &= u_{3, \beta}^{C_i} - \frac{3\Delta t}{2\hat{\omega}_1 |C_i|} [F_{i3}(u_{3, \beta}^{C_i}, u_{2, \beta}^{C_i}, -\mathbf{n}_{i3}) + F_{i3}(u_{3, \beta}^{C_i}, u_{3, \beta}^{C_{i3}}, \mathbf{n}_{i3})]. \end{aligned}$$

Under the assumption that the first order method (89) is non-decreasing in each argument, i.e., monotone, under the CFL condition (90), we have that each $H_{l_e, \beta}$ is non-decreasing under (93). Finally, we combine this with (92) and obtain the maximum principle for high-order methods on triangular grids. \square

So far, we have only dealt with the polynomial case. However, the results also hold for the non-polynomial case with the definition

$$p_R = \frac{U_C}{\omega_R} - \sum_{\beta=1}^{k+1} \sum_{l_e=1}^3 \frac{2}{3} \omega_\beta \hat{\omega}_1 \frac{U_C}{\omega_R} u_{l_e, \beta}^C. \quad (95)$$

4.4.1. Maximum principle satisfying limiter on triangular grids

Let us consider a general reconstruction $r_{C_i} : \mathbb{R}^2 \rightarrow \mathbb{R}$ for the solution in the cell C_i . In the case that the reconstruction r_{C_i} does not satisfy (92), we can modify it in the same way as in one dimension. We define

$$\tilde{r}_{C_i}(\mathbf{x}) = \tilde{\theta}(r_{C_i}(\mathbf{x}) - U_i^n) + U_i^n, \quad \tilde{u}_{\min} = \min \left\{ p_R, u_{l_e, \beta}^{C_i} \mid l_e = 1, 2, 3, \beta = 1, \dots, k + 1 \right\}, \quad (96)$$

$$\tilde{\theta} = \min \left\{ \left| \frac{U_i^n - m}{U_i^n - \tilde{u}_{\min}} \right|, \left| \frac{U_i^n - M}{U_i^n - \tilde{u}_{\max}} \right|, 1 \right\}, \quad \tilde{u}_{\max} = \max \left\{ p_R, u_{l_e, \beta}^{C_i} \mid l_e = 1, 2, 3, \beta = 1, \dots, k + 1 \right\}, \quad (97)$$

with $u_{l_e, \beta}^{C_i} = r_{C_i}(\mathbf{x}_{l_e, \beta})$. The results from one dimension can be transferred to two dimensions directly and are summarized in the following Lemma.

Lemma 4.5. *The maximum principle preserving limiter (96) with (97) is conservative, of high order, and satisfies the maximum preserving condition (92).*

4.5. High-order positivity preserving scheme for the Euler equations

The maximum principle does not hold for systems of equations. However, to solve the Euler equations we need to ensure positivity of the density and pressure. Therefore, we adapt the idea from [33] to the maximum preserving limiter introduced above. Let us consider the two-dimensional Euler equations with the flux

$$f_i(\mathbf{u}) = \begin{pmatrix} m_i \\ \frac{m_i m_1}{\rho} + p \delta_{i1} \\ \frac{m_i m_2}{\rho} + p \delta_{i2} \\ \frac{m_i}{\rho} (E + p) \end{pmatrix}, \quad (98)$$

where δ_{ij} is the Kronecker delta function and with the additional variables $\mathbf{u} = (\rho, m_1, m_2, E)^T$, the density ρ , the mass flux m_1 and m_2 in x - and y -direction, respectively, the total energy E , and the pressure $p = \mathcal{R}\rho T = (\gamma - 1)\left(E - \frac{1}{2} \frac{m_1^2 + m_2^2}{\rho}\right)$ assuming an ideal gas with the ratio of specific heat γ . The method is based on a positivity preserving first order method (88). Further, we use that the pressure p is concave with respect to ρ, m_1, m_2 and E under the condition $\rho > 0$. Thus, the set of admissible states

$$G = \left\{ (\rho, m_1, m_2, E)^T \mid \rho > 0, p > 0 \right\}, \quad (99)$$

is convex. We denote the cell average values at time t_n as $\mathbf{Q}_C^n = (\bar{\rho}_C^n, \bar{m}_{1,C}^n, \bar{m}_{2,C}^n, \bar{E}_C^n)^T$ and the high-order reconstructions in the cell C as

$$\mathbf{q}_C(\mathbf{x}) = (\rho_C(\mathbf{x}), m_{1C}(\mathbf{x}), m_{2C}(\mathbf{x}), E_C(\mathbf{x}))^T. \quad (100)$$

To preserve positivity of the density we proceed in the same way as to preserve the maximum and define the limiter

$$\tilde{\rho}_C(\mathbf{x}) = \tilde{\theta}_1 (\rho_C(\mathbf{x}) - \bar{\rho}_i^n) + \bar{\rho}_i^n, \quad (101)$$

$$\tilde{\theta}_1 = \min \left\{ \left| \frac{\bar{\rho}_i^n - \varepsilon}{\bar{\rho}_i^n - \tilde{\rho}_{\min}} \right|, 1 \right\}, \quad \tilde{\rho}_{\min} = \min \left\{ \rho_R, \rho_{l_e, \beta}^C \mid l_e = 1, 2, 3, \beta = 1, \dots, k + 1 \right\}, \quad (102)$$

with the small threshold $\varepsilon > 0$, and set

$$\tilde{\mathbf{q}}_C(\mathbf{x}) = (\tilde{\rho}_C(\mathbf{x}), m_{1C}(\mathbf{x}), m_{2C}(\mathbf{x}), E_C(\mathbf{x}))^T. \quad (103)$$

To preserve positivity of the pressure p we define

$$t(\mathbf{x}) = \begin{cases} 1, & \text{if } p(\tilde{\mathbf{q}}_C(\mathbf{x})) \geq \varepsilon, \\ t_0 \text{ such that } p(\mathbf{s}_\mathbf{x}(t_0)) = \varepsilon, & \text{if } p(\tilde{\mathbf{q}}_C(\mathbf{x})) < \varepsilon, \end{cases} \quad \mathbf{s}_\mathbf{x}(t) = (1 - t)\mathbf{Q}_C^n + t\tilde{\mathbf{q}}_C(\mathbf{x}). \quad (104)$$

Further, we define the remainder $\tilde{\mathbf{q}}_R = \mathbf{Q}_C^n - \sum_{\beta=1}^{k+1} \sum_{l_e=1}^3 \frac{2}{3} \frac{\omega_\beta \hat{\omega}_1}{\omega_R} \tilde{\mathbf{q}}_C(\mathbf{x}_{l_e, \beta})$ and

$$t_R = \begin{cases} 1, & \text{if } p(\tilde{\mathbf{q}}_R) \geq \varepsilon, \\ t_0 \text{ such that } p(\mathbf{s}_R(t_0)) = \varepsilon, & \text{if } p(\tilde{\mathbf{q}}_R) < \varepsilon, \end{cases} \quad \mathbf{s}_R(t) = (1 - t)\mathbf{Q}_C^n + t\tilde{\mathbf{q}}_R. \quad (105)$$

This allows us to define the new vector of reconstruction functions

$$\tilde{\tilde{\mathbf{q}}}_C(\mathbf{x}) = \theta_2 (\tilde{\mathbf{q}}_C(\mathbf{x}) - \mathbf{Q}_C^n) + \mathbf{Q}_C^n, \quad \text{with} \quad \theta_2 = \min \left\{ \min_{\mathbf{x} \in S_k^{C, \text{edg}}} t(\mathbf{x}), t_R \right\}. \quad (106)$$

We have the following lemma.

Lemma 4.6. *Given the limiter (101) and (106) the (non-polynomial) reconstruction $\tilde{\tilde{\mathbf{q}}}_C$ is of high-order accuracy, conservative, and preserves positivity of the density and pressure.*

Proof. For the first step, using the limiter of the density, we take the results from the maximum preserving limiter. Also the positivity of the pressure and the conservation property of the second limiter (106) are clear. The only open question is the high-order accuracy of the second step.

Let us keep in mind that the original limiter by Zhang and Shu [33] is based on the minimum over all quadrature nodes

$$\hat{\theta}_2 = \min_{\mathbf{x} \in S_k^C} t(\mathbf{x}). \quad (107)$$

We define the vector of polynomials \mathbf{p}_C such that $\mathbf{p}_C(\mathbf{x}) = \tilde{\mathbf{q}}_C(\mathbf{x})$ for all $\mathbf{x} \in S_k^C$. Thus, the values of θ_2 and $\hat{\theta}_2$ are the same for the polynomial reconstruction \mathbf{p}_C and the non-polynomial reconstruction $\tilde{\mathbf{q}}_C$. Furthermore, we know

$$\tilde{\mathbf{q}}_R = \mathbf{Q}_C^n - \sum_{\beta=1}^{k+1} \sum_{i=1}^3 \frac{2}{3} \frac{\omega_\beta \hat{\omega}_1}{\omega_R} \tilde{\mathbf{q}}_C(\mathbf{x}_{i,\beta}) = \mathbf{Q}_C^n - \sum_{\beta=1}^{k+1} \sum_{i=1}^3 \frac{2}{3} \frac{\omega_\beta \hat{\omega}_1}{\omega_R} \mathbf{p}_C(\mathbf{x}_{i,\beta}) = \sum_{\mathbf{x} \in S_k^{C,int}} \frac{\omega_x}{\omega_R} \mathbf{p}_C(\mathbf{x}), \tag{108}$$

which is a convex combination of the values $\mathbf{p}_C(\mathbf{x})$ for $\mathbf{x} \in S_k^{C,int}$. Thus, we obtain

$$p((1 - \hat{\theta}_2)\mathbf{Q}_C^n + \hat{\theta}_2 \tilde{\mathbf{q}}_R) = p\left((1 - \hat{\theta}_2)\mathbf{Q}_C^n + \hat{\theta}_2 \sum_{\mathbf{x} \in S_k^{C,int}} \frac{\omega_x}{\omega_R} \mathbf{p}_C(\mathbf{x})\right) = p\left(\sum_{\mathbf{x} \in S_k^{C,int}} \frac{\omega_x}{\omega_R} ((1 - \hat{\theta}_2)\mathbf{Q}_C^n + \hat{\theta}_2 \mathbf{p}_C(\mathbf{x}))\right), \tag{109}$$

$$\geq \sum_{\mathbf{x} \in S_k^{C,int}} \frac{\omega_x}{\omega_R} p\left((1 - \hat{\theta}_2)\mathbf{Q}_C^n + \hat{\theta}_2 \mathbf{p}_C(\mathbf{x})\right) \geq \varepsilon, \tag{110}$$

since p is concave. We conclude that $\theta_2 \geq \hat{\theta}_2$. Finally, we use the estimate in (74)

$$|\tilde{\mathbf{q}}_C(\mathbf{x}) - \mathbf{q}_C(\mathbf{x})| \leq |\tilde{\mathbf{q}}_C(\mathbf{x}) - \tilde{\mathbf{p}}_C(\mathbf{x})| + |\tilde{\mathbf{p}}_C(\mathbf{x}) - \mathbf{p}_C(\mathbf{x})| + |\mathbf{p}_C(\mathbf{x}) - \mathbf{q}_C(\mathbf{x})|,$$

with

$$|\mathbf{q}_C(\mathbf{x}) - \mathbf{p}_C(\mathbf{x})| = \mathcal{O}(\Delta \mathbf{x}^{k+1}), \tag{111}$$

$$|\tilde{\mathbf{q}}_C(\mathbf{x}) - \tilde{\mathbf{p}}_C(\mathbf{x})| = \theta_2 |\mathbf{q}_C(\mathbf{x}) - \mathbf{p}_C(\mathbf{x})| = \mathcal{O}(\Delta \mathbf{x}^{k+1}), \tag{112}$$

$$|\tilde{\mathbf{p}}_C(\mathbf{x}) - \mathbf{p}_C(\mathbf{x})| = |1 - \theta_2| |\mathbf{p}_C(\mathbf{x}) - \mathbf{Q}_C^n| \leq |1 - \hat{\theta}_2| |\mathbf{p}_C(\mathbf{x}) - \mathbf{Q}_C^n| = |\hat{\mathbf{p}}_C(\mathbf{x}) - \mathbf{p}_C(\mathbf{x})| = \mathcal{O}(\Delta \mathbf{x}^{k+1}), \tag{113}$$

with the original limiter $\hat{\mathbf{p}}_C$ based on $\hat{\theta}_2$ from [32]. \square

Remark 4.1. The positivity preserving limiter works the same way for the one-dimensional schemes with $S_k^{C_i,edg} = \{x_{i-1/2}, x_{i+1/2}\}$.

5. Numerical results

5.1. Numerical results for one-dimensional problems

Let us take a look at some one-dimensional examples to verify the order of convergence and show the ability to deal with challenging one-dimensional problems.

5.1.1. Linear advection equation

To confirm the order of convergence in Theorem 3.1, we consider the linear advection equation

$$\begin{aligned} u_t + au_x &= 0, \\ u(x, 0) &= u_0(x), \quad \text{for } -\infty < x < \infty, \end{aligned} \tag{114}$$

with periodic boundary conditions on the domain $[-1, 1]$ and a wave speed $a = 1$. Next, we consider two different hybrid grids. The structured hybrid grid consists of N cells split equally into two grids $\{x_0, \dots, x_{N/2}\}$ and $\{x_{N/2}, \dots, x_N\}$ with $x_i = \frac{2i}{N} - 1$. The unstructured hybrid grid consists of the unstructured part $\{\tilde{x}_0, \dots, \tilde{x}_{N/2}\}$ with $\tilde{x}_i = x_i + \varepsilon_i$, $\varepsilon_i \in \mathcal{U}(-\frac{0.1}{N}, \frac{0.1}{N})$ uniformly distributed between $[-\frac{0.1}{N}, \frac{0.1}{N}]$ and the structured one $\{x_{N/2}, \dots, x_N\}$.

The convergence of the hybrid method is generally as expected, see Table 3. We compare the accuracy using the hybrid method with $p_{WENO} = 2 \lfloor \frac{p}{2} \rfloor + 1$ and $p_{WENO} = 2p - 1$. For the 3rd order method we observe a reduced error by around a factor 10 in the case $p_{WENO} = 2p - 1$. Table 4 shows the runtime for the different 3rd order methods. The hybrid methods with $p_{WENO} = 2 \lfloor \frac{p}{2} \rfloor + 1$ and $p_{WENO} = 2p - 1$ have a similar computational complexity and they are a bit faster than the RBF-ENO method. Note that the costs of the stencil selection in the RBF-ENO method in one space dimension are not much more expensive than the WENO method. However, the cost of the two-dimensional stencil selection algorithm is quadratic in the size of the stencil.

Table 3

Convergence rates of the Hybrid ENO method for different grid sizes compared with the RBF-ENO method for the linear advection equation on $[-1, 1]$ at time $T = 0.1$. We use periodic boundary conditions and $u_0(x) = \sin(\pi x)$, CFL = 0.5.

N	Unstructured grid						Structured grid		
	Hybrid $2p - 1$		Hybrid $2 \lfloor p/2 \rfloor + 1$		RBF-ENO p		Hybrid $2p - 1$		
	Error	Rate	Error	Rate	Error	Rate	Error	Rate	
$p = 3$	16	2.32e-03	–	1.79e-02	–	2.99e-03	–	2.54e-03	–
	32	2.46e-04	3.25	3.90e-03	2.16	5.25e-04	2.55	5.63e-04	2.17
	64	6.07e-05	1.95	9.70e-04	2.01	8.20e-05	2.61	4.69e-05	3.58
	128	7.78e-06	3.16	2.26e-04	2.09	1.28e-05	2.68	5.88e-06	2.99
	256	9.38e-07	2.86	3.08e-05	2.84	1.61e-06	3.00	9.10e-07	2.69
	512	1.44e-07	2.7	2.14e-06	3.85	2.64e-07	2.60	1.26e-07	2.85
$p = 4$	16	2.41e-04	–	6.49e-04	–	9.77e-04	–	4.96e-04	–
	32	3.86e-05	2.69	5.37e-05	3.63	6.12e-05	4.09	4.52e-05	3.46
	64	2.71e-06	3.71	2.58e-06	4.31	5.36e-06	3.47	2.20e-06	4.36
	128	1.47e-07	4.21	2.06e-07	3.66	4.31e-07	3.57	1.70e-07	3.69
	256	1.70e-08	3.1	1.57e-08	3.71	2.89e-08	3.89	1.66e-08	3.35
	512	1.48e-09	3.53	1.22e-09	3.68	2.97e-09	3.27	1.51e-09	3.47
$p = 5$	16	1.15e-04	–	3.71e-04	–	2.38e-04	–	2.43e-04	–
	32	6.04e-06	4.10	1.75e-05	4.60	9.96e-06	4.66	7.12e-06	5.09
	64	1.71e-07	5.16	5.98e-07	4.32	2.96e-07	4.93	2.62e-07	4.76
	128	8.19e-09	4.33	1.90e-08	4.50	1.34e-08	4.43	7.19e-09	5.19
	256	4.76e-10	4.14	6.70e-10	4.72	7.36e-10	4.16	3.23e-10	4.45
	512	1.52e-11	4.96	3.18e-11	4.22	3.98e-11	4.21	2.83e-11	4.54

Table 4

Runtime comparison for the 3rd order methods solving the linear advection equation.

	Hybrid $2p - 1$	Hybrid $2 \lfloor p/2 \rfloor + 1$	RBF-ENO p
16	2.7	1.4	0.8
32	4.4	2.5	1.6
64	4.6	3.2	3.2
128	8.4	7.4	8.4
256	18.8	15.8	19.8
512	45.5	44.0	62.6

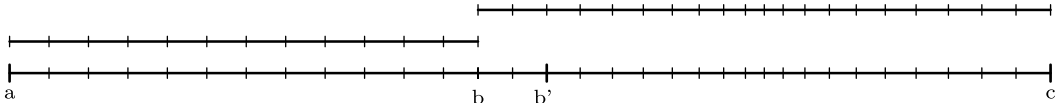


Fig. 9. 1D hybrid grid for Euler equations.

5.1.2. Euler equations

Next, we present numerical results for the one-dimensional Euler equations

$$\begin{pmatrix} \rho \\ m \\ E \end{pmatrix}_t + \begin{pmatrix} m \\ \frac{m^2}{\rho} + p \\ \frac{m}{\rho}(E + p) \end{pmatrix}_x = 0, \tag{115}$$

with the density ρ , the mass flux m , the total energy E , and the pressure $p = \mathcal{R}\rho T = (\gamma - 1)(E - \frac{1}{2} \frac{m^2}{\rho})$ assuming an ideal gas with the ratio of specific heat $\gamma = 1.4$ [27]. We test the behavior of the hybrid RBF-ENO method with shocks, contact discontinuities, and rarefaction waves. The computational grid for the Euler equations is shown in Fig. 9. The goal is to run it on the left half with the structured WENO method and on the right half with a continuously refined grid such that the middle cell is half the size of the outer ones. Note that we have to change the two original meshes in $[a, b']$ and $[b', c]$ by adding the n_{ghost} last cells of the structured mesh to the unstructured one. The following results are based on a grid with $N_1 = 78$ cells in $[a, b]$ and $N_2 = 101$ cells in $[b, c]$. Further, the reconstruction is performed in the characteristic variables $\mathbf{V} = R^{-1}\mathbf{U}$, with the eigenvectors R of the Jacobian of $f(\rho, m, E) = (m, \frac{m^2}{\rho} + p, \frac{m}{\rho}(E + p))^T$.

Sod's shock tube problem. We consider Sod's shock tube problem on the domain $[-5, 5]$ based on the initial conditions

$$(\rho_0, m_0, p_0) = \begin{cases} (1, 0, 1) & \text{if } x < 0 \\ (0.125, 0, 0.1) & \text{if } x \geq 0 \end{cases}, \tag{116}$$

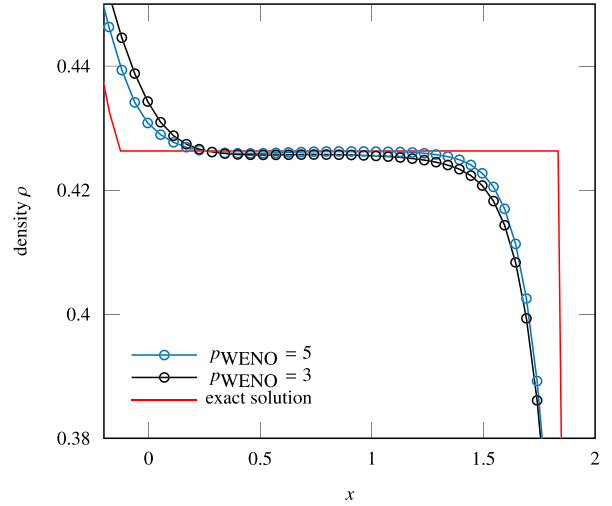
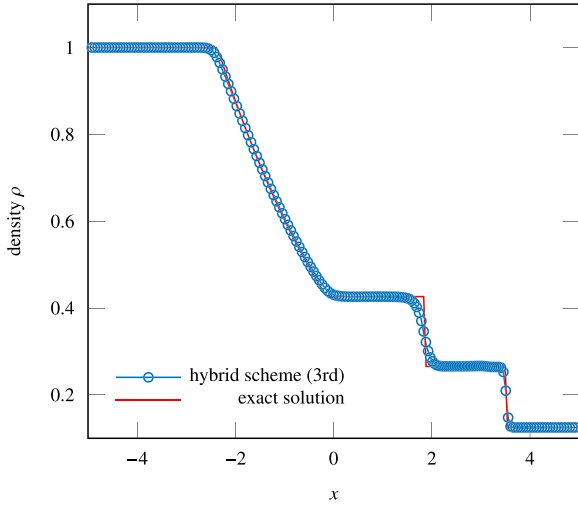


Fig. 10. Sod's shock tube problem on $[-5, 5]$ at time $T = 2$ with $CFL = 0.8$ solved by the hybrid RBF-ENO method of order 3.

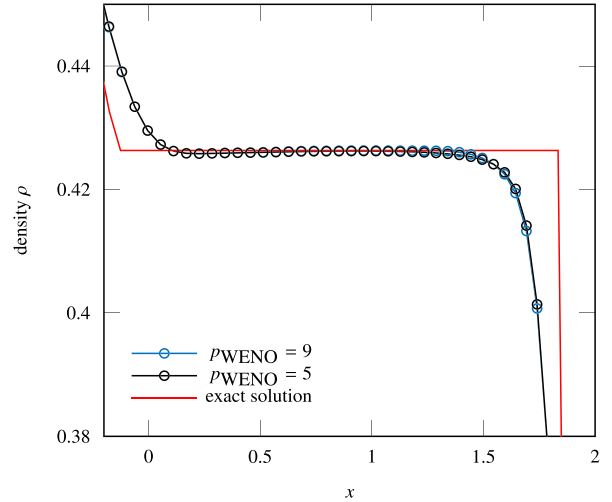
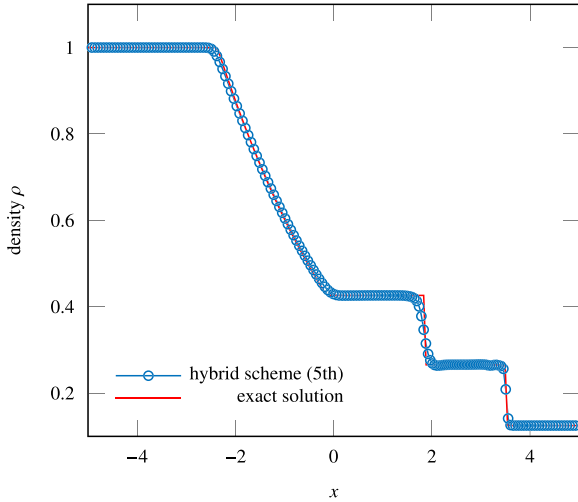


Fig. 11. Sod's shock tube problem on $[-5, 5]$ at time $T = 2$ with $CFL = 0.8$ solved by the hybrid RBF-ENO method of order 5.

where $m = \rho u$. This Riemann problem produces a rarefaction wave, followed by a contact and a shock discontinuity. Fig. 10 shows the results for the hybrid RBF-ENO method of order 3. We observe that the rarefaction wave, the contact discontinuity, and the shock are well resolved. Furthermore, it is clear that the 3rd order method with $p_{WENO} = 5$ resolves the contact discontinuity better. In the case of the 5th order method the differences between $p_{WENO} = 5$ and $p_{WENO} = 9$ are not obvious anymore, Fig. 11.

Shu-Osher shock-entropy wave interaction problem. We consider the Shu-Osher shock-entropy wave interaction problem. This Riemann problem has the initial conditions

$$(\rho_0, m_0, p_0) = \begin{cases} (3.857143, 2.629369, 10.33333) & \text{if } x < -4 \\ (1 + 0.2 \sin(5x), 0, 1) & \text{if } x \geq -4 \end{cases}, \quad (117)$$

and the computational domain $[-5, 5]$. As before, we obtain the correct solution with the 3rd and 5th order method, Fig. 12. In this example, we see a substantial advantage of the high-order methods. There are evident improvements in the resolution of the waves as the order increases.

Two interacting blast waves. As the last one-dimensional example, we test the method on the two interacting blast waves based on the initial conditions

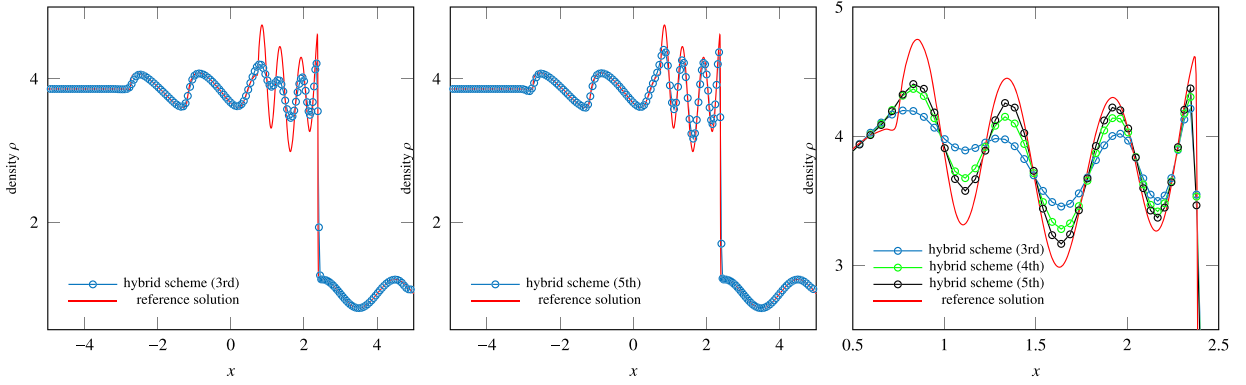


Fig. 12. Shu-Osher problem on $[-5, 5]$ at time $T = 1.8$ with $CFL = 0.8$ solved by the hybrid RBF-ENO method with $p_{WENO} = 2p - 1$.

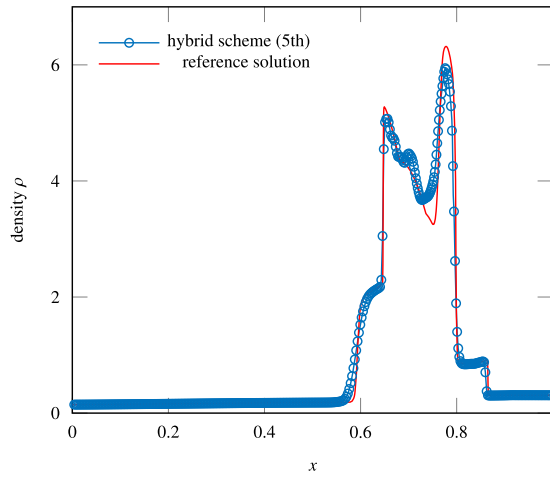


Fig. 13. WC blast wave problem on $[0, 1]$ at time $T = 0.038$ with $N = 200$, $CFL = 0.5$ solved by the hybrid RBF-ENO method of order 5.

$$(\rho_0, m_0, p_0) = \begin{cases} (1, 0, 1000) & \text{if } x < 0.1 \\ (1, 0, 0.01) & \text{if } 0.1 \leq x < 0.9 \\ (1, 0, 100) & \text{if } x \geq 0.9 \end{cases} \quad (118)$$

This problem was introduced by Woodward and Colella [34] and is more challenging due to the collision of the shock waves. In [20], we had some difficulties to solve this problem with the RBF-TeCNOp method. There, we introduced a new symmetric positive definite dissipation operator, which mimics the more dissipative Rusanov-type diffusion operator. Here, we compute the two interacting blast waves with the hybrid RBF-ENO method of order 5 based on the same grid as before with $N_1 = 158$ and $N_2 = 205$. If we use the original version, we obtain negative density or pressure. By using the positivity preserving limiter from Section 4, we stabilize the method and calculate the solution at time $T = 0.038$. The results of the fifth order hybrid RBF-ENO method combined with the positivity preserving limiter are shown in Fig. 13 and show excellent agreement with the reference solution.

5.2. Numerical results for two-dimensional problems

In this section, we demonstrate the hybrid RBF-ENO method on a couple of numerical examples. First, we solve Burgers' equation to compare the complexity of the hybrid and the non-hybrid method. To show the robustness of the method in two dimensions, we conclude with several numerical examples of the two-dimensional Euler equations (98). We start with some known examples to show that the solutions are comparable to the ones generated with the other methods. We conclude the section with the simulation of the scramjet and a model of a conical aerospike nozzle to illustrate the robustness of the scheme. The grids in this section are generated using Gmsh [35] and to specify the grids we introduce the number of triangular cells N_{TRI} and the number of quadrilateral cells N_{QUAD} .

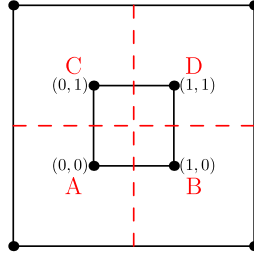
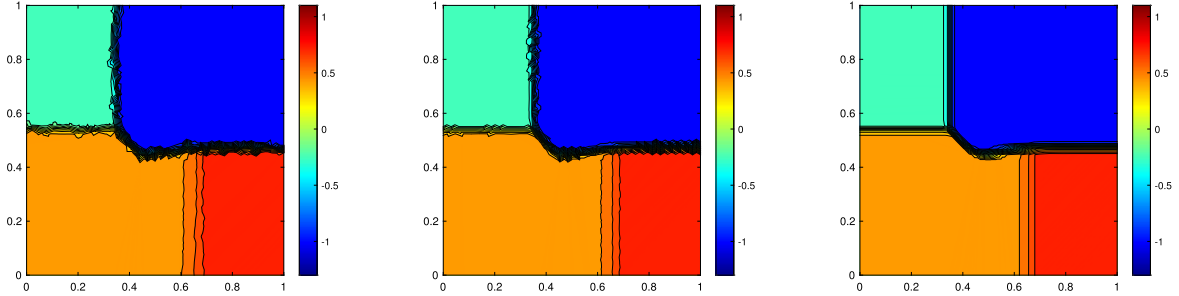


Fig. 14. Domain extension, initial value composition and grid.

Table 5
Runtime comparison for the 3th order methods solving the 2D Burgers' equation on a single core, measured in seconds.

N_{TRI}	Hybrid RBF-ENO	RBF-ENO	Speed-up
155	24	96	4
610	143	810	5.6
1348	411	2925	7.1
2390	947	6840	7.2



(a) Hybrid RBF-ENO of order 3 with $N_{TRI} = 2390$, $N_{QUAD} = 8478$. (b) RBF-ENO of order 3 with $N_{TRI} = 21382$. (c) WENO of order 5 with $N_{QUAD} = 19600$.

Fig. 15. Solution of the Burgers' equation at $T = 0.25$, $CFL = 0.8$.

5.2.1. Burgers' equation

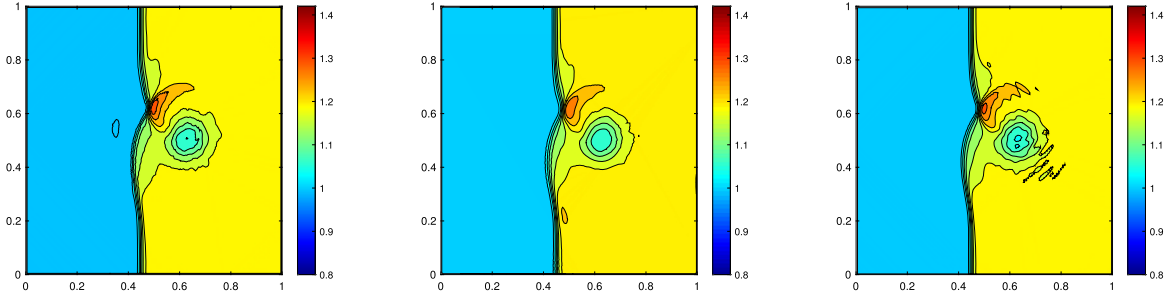
With the Burgers' equation we demonstrate the difference in the computational cost of the hybrid and the non-hybrid RBF-ENO method. We consider Burgers' equation

$$u_t + \frac{1}{2}(u^2)_x + \frac{1}{2}(u^2)_y = 0, \tag{119}$$

on the domain $\Omega = [0, 1]^2$ with the initial conditions

$$u_0 = \begin{cases} -1 & \text{if } x > 0.5, y > 0.5, \\ -0.2 & \text{if } x < 0.5, y > 0.5, \\ 0.5 & \text{if } x < 0.5, y < 0.5, \\ 0.8 & \text{if } x > 0.5, y < 0.5, \end{cases} \tag{120}$$

on the extended domain $[-1, 2] \times [-1, 2]$ to avoid boundary effects, see Fig. 14. The hybrid method is based on the grid from Fig. 6 and the non-hybrid scheme is based on a uniform triangulation. We compare the computational cost depending on the number of triangles N_{TRI} in the target area $[0, 1] \times [0, 1]$. Note that the triangulation for the non-hybrid method has in total around nine times the number of cells. The hybrid method has around one-ninth of triangular cells plus the quadrilateral cells around them. Thus, the upper bound for the speed-up is nine. From Table 5, we get a speed-up of around 7.2 for a fine enough grid. Compared to the one-dimensional linear advection equation, Table 4, we clearly observe the computational advantage of the hybrid RBF-ENO method in multiple dimensions. We do not observe any marginal difference between the solutions of the different methods with $N_{TRI} = 2390$, Fig. 15.



(a) Hybrid RBF-ENO of order 3 with $N_{TRI} = 3408$, $N_{QUAD} = 11700$ and $CFL = 0.8$. (b) RBF-ENO of order 3 with $N_{TRI} = 14616$ and $CFL = 0.5$. (c) WENO of order 5 with $N_{QUAD} = 15876$ and $CFL = 0.8$.

Fig. 16. Shock vortex interaction problem at $T = 0.35$ with 20 contour lines in $[0.8, 1.42]$.

5.2.2. Shock vortex interaction problem

The shock vortex interaction problem is based on the discontinuous initial condition

$$(\rho, m_1, m_2, E) = \begin{cases} (\rho_L, m_{1,L}, m_{2,L}, E_L) & \text{if } x < 0.5, \\ (\rho_R, m_{1,R}, m_{2,R}, E_R) & \text{if } x \geq 0.5, \end{cases} \quad (121)$$

with the left state superposed by the perturbation

$$\begin{aligned} \delta u_1 &= \epsilon \frac{y - u_c}{r_c} \exp(\beta(1 - r^2)), & \delta u_2 &= -\epsilon \frac{x - x_c}{r_c} \exp(\beta(1 - r^2)), \\ \delta \theta &= -\frac{\gamma - 1}{4\beta\gamma} \epsilon^2 \exp(2\beta(1 - r^2)), & \delta s &= 0, \end{aligned} \quad (122)$$

with the temperature $\theta = p/\rho$, the physical entropy $s = \log p - \gamma \log \rho$ and the distance $r^2 = ((x - x_c)^2 + (y - y_c)^2)/r_c^2$. The left state is given by

$$(\rho_L, u_{1,L}, u_{2,L}, E_L) = (1, \sqrt{\gamma}, 0, 1),$$

and the right state by

$$\begin{aligned} p_R &= 1.3, & \rho_R &= \rho_L \left(\frac{\gamma - 1 + (\gamma + 1)p_R}{\gamma + 1 + (\gamma - 1)p_R} \right), \\ u_{1,R} &= \sqrt{\gamma} + \sqrt{2} \left(\frac{1 - p_R}{\sqrt{\gamma - 1 + p_R(\gamma + 1)}} \right), & u_{2,R} &= 0. \end{aligned}$$

We choose the following parameters of the vortex $\epsilon = 0.3$, $r_c = 0.05$, $\beta = 0.204$ with the $(x_c, y_c) = (0.25, 0.5)$. The computational grid is shown in Fig. 6 with $n_{ghost} = 2$ in $[0, 1] \times [0, 1]$. The comparison between the hybrid RBF-ENO method, the RBF-ENO method of order 3 and the WENO method of order 5 shows a similar behavior, Fig. 16. We compare the 3rd order methods with the 5th order WENO method since we use it also in the hybrid method. Both the shock and the vortex are resolved in a similar way.

5.2.3. Transonic flow past NACA-0012 airfoil

The NACA-0012 is a two-dimensional cross section of an airfoil for aircraft wing. It is based on the first systematic tests of airfoils in a wind tunnel. The NACA-0012 is a common test case for numerical solvers. It has no camber and a ratio of profile thickness to chord length of 0.12. The transonic simulation of a NACA-0012 airfoil in a freestream of Mach number $M_\infty = 0.85$ with an angle of attack α builds one shock at the top and one at the bottom of the airfoil. The hybrid grid is build as above. We have eight QUAD patches, a TRI one in the center of the grid and some Q2Q, Q2T and RT connection patches. The whole grid is of the size $[-2, 15] \times [-8, 8]$ with the triangular grid inside $[-0.2, 1.5] \times [-0.8, 0.8]$ and it consists of 199 points on the airfoil, $N_{QUAD} = 169036$ quadrilaterals and $N_{TRI} = 10012$ triangles. The central part of the grid with its triangulation is shown in Fig. 17. The solution with an angle of attack $\alpha = 0^\circ$ of the hybrid RBF-ENO method of order 3 is shown in Fig. 18(a). We observe the characteristic steady shock waves at the top and the bottom of the surface of the airfoil, which are comparable to the results in [36]. For an angle of attack $\alpha = 2^\circ$ we show the Mach number of the solution in Fig. 18(b). The dimensionless pressure coefficient

$$C_p = \frac{2}{\gamma M_\infty^2} \left(\frac{p}{p_\infty} - 1 \right), \quad (123)$$

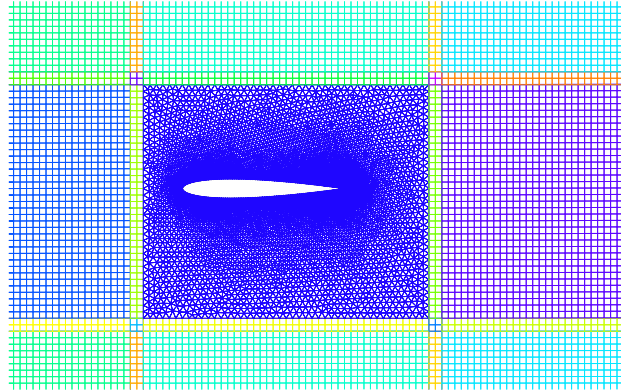


Fig. 17. Hybrid grid for the Airfoil NACA-0012.

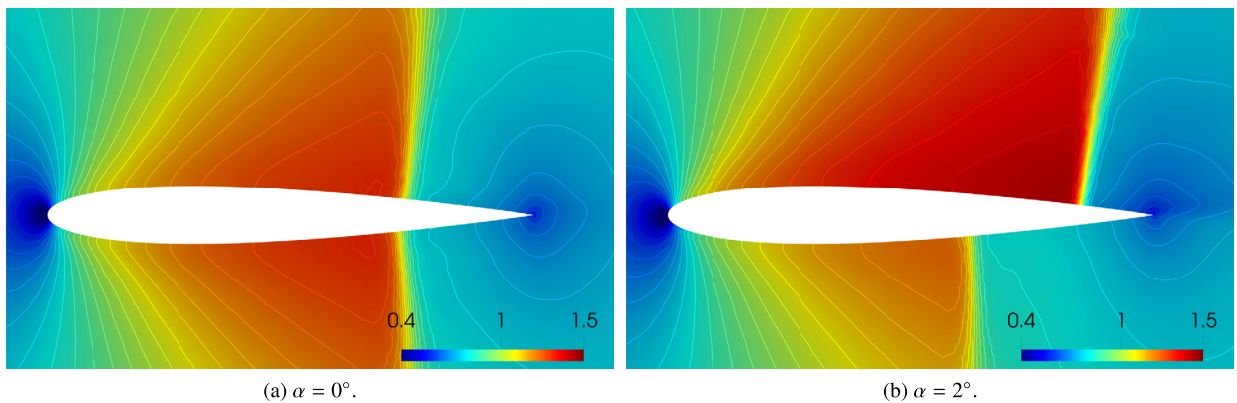


Fig. 18. Mach number of the Airfoil NACA-0012 problem by the hybrid RBF-ENO method of order 3 with CFL = 0.8 and 30 contour lines between 0.4 and 1.5.

with the farfield pressure p_∞ and the pressure $p = p(x)$ is often used in aerodynamics and hydrodynamics to test engineering models. The pressure coefficient at the surface of the airfoil is shown in Fig. 19. For zero degree angle of attack, we observe a qualitatively similar solution to that in [36], see Fig. 19(a).

5.2.4. Scramjet flow model

The supersonic combustion ramjet (scramjet) is based on the ramjet engine. The idea is to avoid the deceleration before the combustion to increase its efficiency at high speeds. Similar to the ramjet it requires hypersonic initial speed and must therefore be accelerated by other jet engines. It finds application in modern airbreathing cruise or acceleration vehicle with the scramjet engine at the bottom [37]. More details can be found in [38,39].

We are simulating the two-strut scramjet [40–44] with the geometrical details from [45]. However, due to the symmetry we use just the upper half with symmetric boundary conditions, Fig. 20 with the coordinates in Table 6. In the first experiment, we enforce a Mach 3 inflow at the inlet between the points 1 and 2 and outflow boundary conditions at the outlet between the points 4 and 5. At the real walls we apply slip wall boundary conditions [46] and symmetric boundary conditions between the points 1 and 5. Kumar [40] simulates the scramjet engine solving the full Navier-Stokes equations. We are interested in the shock capturing of the method and therefore consider the inviscid Euler equations (98). The simulation is performed on a grid based on the division into patches shown in Fig. 21 with $N_{TRI} = 5036$ and $N_{QUAD} = 14939$ and the grid looks similar to the example in Fig. 22. It is generated using the frontal Delaunay option in Gmsh. The solution of the hybrid RBF-ENO method, shown in Fig. 23, compares well with the result in [45].

Following Eberle et al. [41] we also model the more difficult problem with a Mach 10 inflow. Due to the strong shock waves, we get negative density and pressure with the original hybrid RBF-ENO method. Hence, we need the positivity preserving limiter described in Section 4. The solution of the Mach 10 inflow problem, Fig. 24, compares well with the result from [41].

5.2.5. Flow through conical aerospike nozzle

One approach to create thrust is the conical aerospike nozzle [47]. As a final example we consider nozzle jet flow simulations of a conical aerospike nozzle. Different from the bell nozzle the aerospike nozzle is an annular nozzle and

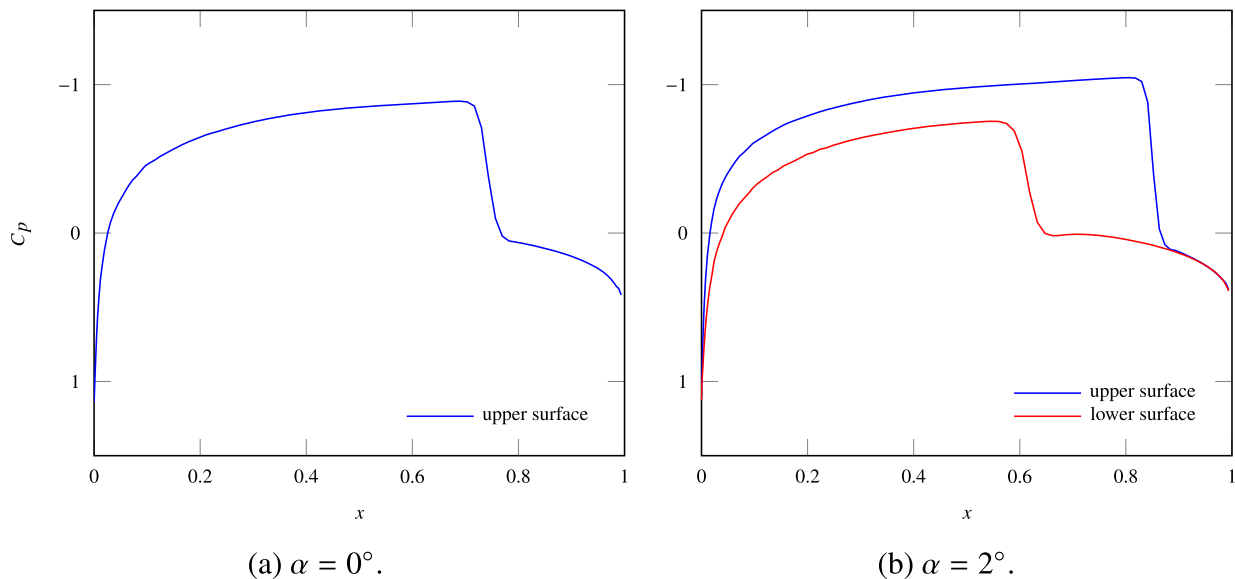


Fig. 19. Pressure coefficient at the surface of the airfoil.

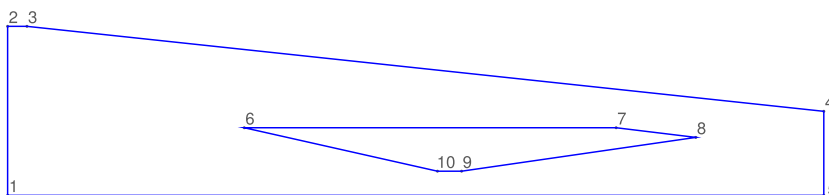


Fig. 20. Geometry of the scramjet model from [45].

Table 6
Coordinates defining the geometry of the scramjet model from [45].

Points	1	2	3	4	5	6	7	8	9	10
x-Coord	0	0	0.4	16.9	16.9	4.9	12.6	14.25	9.4	8.9
y-Coord	0	3.5	3.5	1.74	0	1.4	1.4	1.2	0.5	0.5

it develops the thrust against the outer surface of the conical plug at its center. At design pressure the efficiency of the aerospike nozzle is the same as for the bell nozzle. However, in the case of lower and higher outer pressure the aerospike nozzle is more efficient. This advantage comes with a high price of construction complexity. An improvement of this concept is the aerospike nozzle with a truncated plug. The lost thrust is compensated by additional cold air injected at the truncation face, called base bleed. More precisely, the pressure in this cold gas area, which is acting on the truncated face, adds the additional thrust. This concept appears to give promising results for the development of reusable launch vehicles such as Single-Stage-To-Orbit or Two-Stage-To-Orbit systems.

In recent years, multiple studies of conical aerospike nozzles have been done [48–53]. This numerical example is based on an experiment by Verma [54] with a linear plug geometry, Fig. 25 with the coordinates in Table 7. Based on the experiments of Verma, multiple numerical studies were carried out [55–57]. These studies analyze the shock-boundary layer interaction and use the axisymmetric Navier-Stokes equations. As for the scramjet simulation we consider the 3rd order method with the shock waves and use the axisymmetric Euler equations.

Axisymmetric Euler equations. The axisymmetric Euler equations are expressed in cylindrical coordinates and they can be written with or without swirling flows [58]. Let us assume the Euler equations in three space dimensions with the variables $\mathbf{x} = (x_1, x_2, x_3)^T \in \mathbb{R}^3$

$$\frac{\partial \mathbf{u}}{\partial t} + \sum_{i=1}^3 \frac{\partial}{\partial x_i} f_i(\mathbf{u}), \tag{124}$$

with $\mathbf{u} = (\rho, m_1, m_2, m_3, E)^T$ and

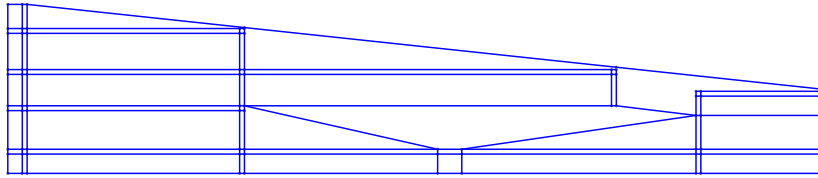


Fig. 21. Scheme for hybrid grid for scramjet model.

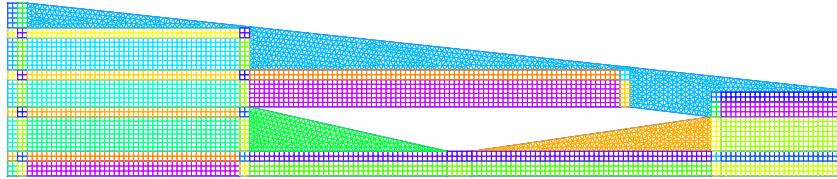


Fig. 22. Grid with the double grid size.

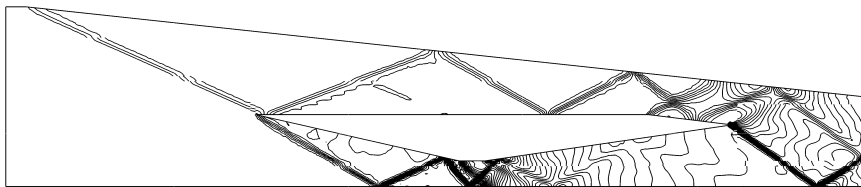


Fig. 23. Density in the scramjet engine with Mach 3 inflow by the hybrid RBF-ENO method of order 3 with CFL = 0.8 with 50 contour lines between 1.0 and 6.0.

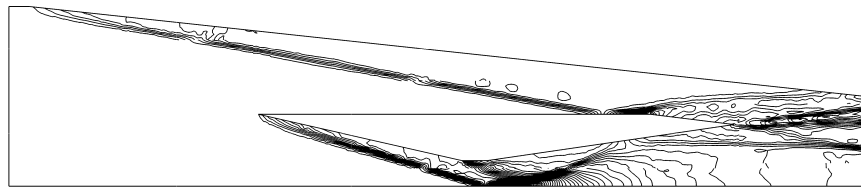


Fig. 24. Density in the scramjet engine with Mach 10 inflow by the hybrid RBF-ENO method of order 3 with CFL = 0.8 with 50 contour lines between 0.0 and 11.0.

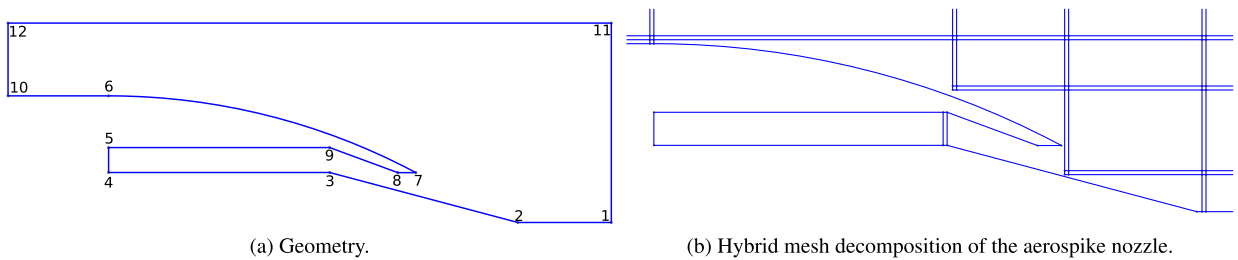


Fig. 25. Nozzle geometry and mesh generation.

$$f_i(\mathbf{u}) = \begin{pmatrix} m_i \\ \frac{m_i m_1}{\rho} + p \delta_{i1} \\ \frac{m_i m_2}{\rho} + p \delta_{i2} \\ \frac{m_i m_3}{\rho} + p \delta_{i3} \\ \frac{m_i}{\rho} (E + p) \end{pmatrix}. \tag{125}$$

The axisymmetric Euler equations are based on the cylindrical coordinates (x, r, θ) and the relation

$$(x_1, x_2, x_3) = (x, r \cos \theta, r \sin \theta), \tag{126}$$

Table 7

Coordinates defining the geometry of the nozzle from [57] with $A = 25.0705074$ and $D = 50$. The curved line is a circular segment with radius $R = \frac{152.8^2 + 38.5^2}{2 \times 38.5}$.

Points	1	2	3	4	5	6	7	8	9	10	11	12
x-Coord	$25D$	203.51	109.95	0	0	0	152.8	143.8	109.95	$-5D$	$25D$	$-5D$
y-Coord	0	0	4.5	A	$A + 12.5$	63.5	25	25	$A + 12.5$	63.5	$5D$	$5D$

with the symmetry assumption around the x -axis all terms with partial derivative in θ are zero. This gives the following system of equations

$$\frac{\partial \hat{\mathbf{u}}}{\partial t} + \frac{\partial}{\partial x} f_x(\hat{\mathbf{u}}) + \frac{\partial}{\partial r} f_r(\hat{\mathbf{u}}) = H(\hat{\mathbf{u}}), \tag{127}$$

with $\hat{\mathbf{u}} = (\rho, m_x, m_r, m_\theta, E_S)^T$ and

$$f_x(\hat{\mathbf{u}}) = \begin{pmatrix} m_x \\ \frac{m_x^2}{\rho} + p \\ \frac{m_x m_r}{\rho} \\ \frac{m_x m_\theta}{\rho} \\ \frac{m_x}{\rho} (E_S + p) \end{pmatrix}, \quad f_r(\hat{\mathbf{u}}) = \begin{pmatrix} m_r \\ \frac{m_r m_x}{\rho} \\ \frac{m_r^2}{\rho} + p \\ \frac{m_r m_\theta}{\rho} \\ \frac{m_r}{\rho} (E_S + p) \end{pmatrix}, \quad H(\hat{\mathbf{u}}) = -\frac{1}{r} \begin{pmatrix} m_r \\ \frac{m_r m_x}{\rho} \\ \frac{m_r^2 - m_\theta^2}{\rho} \\ 2 \frac{m_r m_\theta}{\rho} \\ \frac{m_r}{\rho} (E_S + p) \end{pmatrix},$$

with $E_S = E - \frac{1}{2} u_\theta^2$ [58].

Note that even if we assume that the derivatives in θ are zero, the axisymmetric Euler equations (127) include swirling flows $u_\theta \neq 0$. Thus, we have a two-dimensional system of equations of size five.

In the simplified case without swirling flows, we assume $u_\theta = 0$ and obtain

$$\frac{\partial \tilde{\mathbf{u}}}{\partial t} + \frac{\partial}{\partial x} \tilde{f}_x(\tilde{\mathbf{u}}) + \frac{\partial}{\partial r} \tilde{f}_r(\tilde{\mathbf{u}}) = \tilde{H}(\tilde{\mathbf{u}}), \tag{128}$$

with $\tilde{\mathbf{u}} = (\rho, m_x, m_r, E_S)^T$ and

$$\tilde{f}_x(\tilde{\mathbf{u}}) = \begin{pmatrix} m_x \\ \frac{m_x^2}{\rho} + p \\ \frac{m_x m_r}{\rho} \\ \frac{m_x}{\rho} (E_S + p) \end{pmatrix}, \quad \tilde{f}_r(\tilde{\mathbf{u}}) = \begin{pmatrix} m_r \\ \frac{m_r m_x}{\rho} \\ \frac{m_r^2}{\rho} + p \\ \frac{m_r}{\rho} (E_S + p) \end{pmatrix}, \quad \tilde{H}(\tilde{\mathbf{u}}) = -\frac{1}{r} \begin{pmatrix} m_r \\ \frac{m_r m_x}{\rho} \\ \frac{m_r^2}{\rho} \\ \frac{m_r}{\rho} (E_S + p) \end{pmatrix}.$$

This system of equations is equivalent to the two-dimensional Euler equations (98) with the additional source term \tilde{H} .

High-order source term. To solve hyperbolic conservation laws with a source term

$$\mathbf{u}_t + \sum_{i=1}^d f_i(\mathbf{u})_{x_i} = G(\mathbf{u}, \mathbf{x}, t), \quad (\mathbf{x}, t) \in \mathbb{R}^d \times \mathbb{R}_+, \tag{129}$$

$$\mathbf{u}(0) = \mathbf{u}_0,$$

with the source term G , we can use the finite volume method (4) and add an approximation of the average source term over the cell C_i

$$\frac{dU_i}{dt} + \frac{1}{|C_i|} \sum_{l \in \mathcal{E}} F_{il_e} = G_i, \quad G_i = \frac{1}{|C_i|} \int_{C_i} G(\mathbf{u}, \mathbf{x}, t) d\mathbf{x} + \mathcal{O}(\Delta \mathbf{x}^p). \tag{130}$$

For a first order method we use

$$G_i = G(\mathbf{U}_i, \mathbf{x}_{M,i}, t), \tag{131}$$

with the midpoint $\mathbf{x}_{M,i}$ of the cell C_i . In the case of higher order methods, we need to distinguish between triangular cells and the quadrilaterals. For triangular cells using the RBF-ENO reconstruction, we make use of the high-order reconstruction s_i from the ENO step and evaluate it at the two-dimensional symmetric Gaussian quadrature points \mathbf{x}_k of order p for triangles

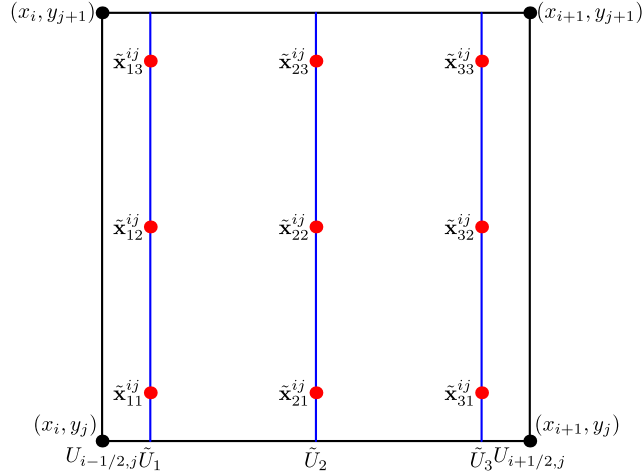


Fig. 26. Principle of 2D quadrilateral quadrature for $n_Q = 3$.

$$G_i = \sum_{k=1}^{n_Q} \omega_k G(s_i(\tilde{\mathbf{x}}_k), \mathbf{x}_k, t), \tag{132}$$

with its quadrature weights ω_k and points $\tilde{\mathbf{x}}_k$ [59]. The additional evaluations of the reconstruction increase the cost only marginally. In the case of quadrilateral cells, we can not use the same technique since we never construct the explicit polynomial. However, we can adapt the technique introduced by Buchmüller and Helzel [29].

Let us assume the cell

$$C_{ij} = \left\{ (x_{i-1/2}, y_{j-1/2}), (x_{i-1/2}, y_{j+1/2}), (x_{i+1/2}, y_{j-1/2}), (x_{i+1/2}, y_{j+1/2}) \right\},$$

with $i, j \in \mathbb{N}$. For a high-order approximation of the integral of the source term, based on a quadrature rule in one dimension, we seek

$$G_{ij} = \frac{1}{\Delta x \Delta y} \int_{x_{i-1/2}}^{x_{i+1/2}} \int_{y_{j-1/2}}^{y_{j+1/2}} G(\mathbf{u}, (x, y), t) dy dx \approx \sum_{k=1}^{n_Q} \sum_{l=1}^{n_Q} \omega_k \omega_l G(\mathbf{u}(\tilde{\mathbf{x}}_{kl}^{ij}), \tilde{\mathbf{x}}_{kl}^{ij}, t), \tag{133}$$

with the quadrature nodes $\tilde{\mathbf{x}}_{kl}^{ij} = (x_{ik}, y_{jl})$ for $k, l = 1, \dots, n_Q$. Thus, the goal is to find a high-order approximation of $\mathbf{u}(\tilde{\mathbf{x}}_{kl}^{ij})$ in terms of the average cell values $\mathbf{U}_{i,j}$, see Fig. 26. In a first step, we express the edge averages at the quadrature nodes x_{ik}

$$\tilde{\mathbf{U}}_k^{ij} = \frac{1}{\Delta y} \int_{y_{j-1/2}}^{y_{j+1/2}} \mathbf{u}(x_{ik}, y) dy = \tilde{\mathbf{U}}_k(\dots, \mathbf{U}_{i,j}, \mathbf{U}_{i+1,j}, \dots) + \mathcal{O}(\Delta x^p), \tag{134}$$

in terms of cell averages $\mathbf{U}_{i,j}$. In the second step, we estimate

$$\mathbf{u}(\tilde{\mathbf{x}}_{kl}^{ij}) = \tilde{\mathbf{u}}_l(\dots, \tilde{\mathbf{U}}_k^{ij}, \dots) + \mathcal{O}(\Delta y^p), \tag{135}$$

with the edge averages $\tilde{\mathbf{U}}_k^{ij}$ for $k \in \mathbb{N}$.

Example 5.1. In the case of Gauss-Legendre integration with $n_Q = 3$, we have the following approximations

$$\begin{aligned} \tilde{\mathbf{U}}_1^{ij} &= \frac{\mathbf{U}_{i-1,j}}{4\sqrt{3}} + \mathbf{U}_{i,j} - \frac{\mathbf{U}_{i+1,j}}{4\sqrt{3}} + \mathcal{O}(\Delta x^p), \\ \tilde{\mathbf{U}}_2^{ij} &= \frac{-\mathbf{U}_{i-1,j}}{24} + \frac{26\mathbf{U}_{i,j}}{24} - \frac{\mathbf{U}_{i+1,j}}{24} + \mathcal{O}(\Delta x^p), \\ \tilde{\mathbf{U}}_3^{ij} &= \frac{-\mathbf{U}_{i-1,j}}{4\sqrt{3}} + \mathbf{U}_{i,j} + \frac{\mathbf{U}_{i+1,j}}{4\sqrt{3}} + \mathcal{O}(\Delta x^p), \end{aligned}$$

for the edge averages. For the evaluation at the quadrature points we have

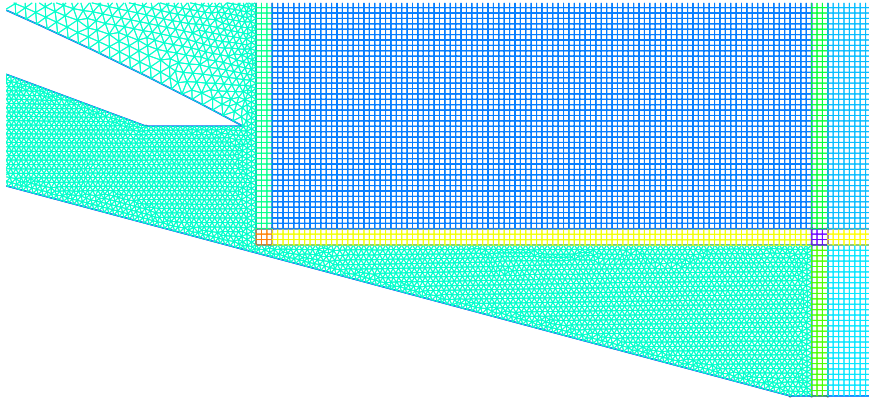


Fig. 27. Hybrid mesh at the nozzle exit.

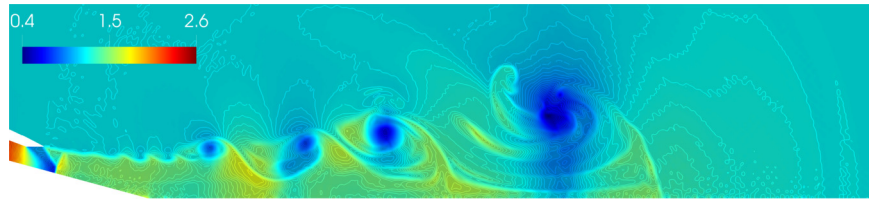


Fig. 28. Density of conical aerospike nozzle with NPR = 2.1.

$$\begin{aligned} \mathbf{u}(\tilde{\mathbf{x}}_{k1}^{ij}) &= \frac{\tilde{\mathbf{U}}_k^{ij-1}}{4\sqrt{3}} + \tilde{\mathbf{U}}_k^{ij} - \frac{\tilde{\mathbf{U}}_k^{ij+1}}{4\sqrt{3}} + \mathcal{O}(\Delta x^p) + \mathcal{O}(\Delta y^p), \\ \mathbf{u}(\tilde{\mathbf{x}}_{k2}^{ij}) &= \frac{-\tilde{\mathbf{U}}_k^{ij-1}}{24} + \frac{26\tilde{\mathbf{U}}_k^{ij}}{24} - \frac{\tilde{\mathbf{U}}_k^{ij+1}}{24} + \mathcal{O}(\Delta x^p) + \mathcal{O}(\Delta y^p), \\ \mathbf{u}(\tilde{\mathbf{x}}_{k3}^{ij}) &= \frac{-\tilde{\mathbf{U}}_k^{ij-1}}{4\sqrt{3}} + \tilde{\mathbf{U}}_k^{ij} + \frac{\tilde{\mathbf{U}}_k^{ij+1}}{4\sqrt{3}} + \mathcal{O}(\Delta x^p) + \mathcal{O}(\Delta y^p), \end{aligned}$$

with $p = 5$.

Combining the hybrid high-resolution RBF-ENO method with the high-order source term, we can solve the axisymmetric Euler equations (128).

Remark 5.1. The high-order source term evaluation does not reduce oscillations. In principle, this could cause problems like negative density or pressure. However, we never encountered this issue.

Hybrid grid and numerical results. We discretize the geometry of the conical aerospike nozzle given by Fig. 25. The triangular part of the hybrid grid includes the nozzle exit and its outer curved surface. The remaining domain is divided into quadrilateral patches. Fig. 25(b) shows the domain division into structured and unstructured patches. A segment of the final mesh at the nozzle exit can be found in Fig. 27. Note that we use $n_{\text{ghost}} = 3$ in this example. This gives us a grid with $N_{\text{TRI}} = 18872$ and $N_{\text{QUAD}} = 1400543$. The boundary conditions are inflow boundary conditions at the inlet between the points 4 and 5, slip wall boundary conditions for the nozzle and symmetric boundary conditions at the origin $r = 0$. The outside is modeled with far-field boundary conditions with the ambient pressure $p_\infty = 101325$ Pa, temperature $T_\infty = 300$ K and zeros speed. The ideal gas law $p = \rho \mathcal{R} T$ with the gas constant $\mathcal{R} = 287.14$ J/kg/K is used to calculate the density. At the inlet we choose the pressure $p_{\text{in}} = \text{NPR} p_\infty$, temperature $T_{\text{in}} = T_\infty$, $u_x = 100$ m/s and $u_r = 0$ with the nozzle pressure ratio NPR.

Based on the results from Nair et al. [57] we simulate the conical aerospike nozzle with NPR = 2.1 and 3.82. The results for the nozzle pressure ratio NPR = 2.1 at time $T = 2$ s are shown in Figs. 28 and 29 with close up view in Fig. 32(a). The Figs. 30 and 31 show the density and the Mach number distribution with NPR = 3.82 at time $T = 2$ s. We need to be aware of the difference between our model and the one from [57] and the uncertainties in the boundary conditions. However, the shock patterns of our results, Fig. 32, are comparable to the results from Nair et al. [57]. In Fig. 32, we observe a discontinuous behavior of the contour lines. This is a rendering artifact coming from the transition between triangular and rectangular patches and does not influence the simulation.

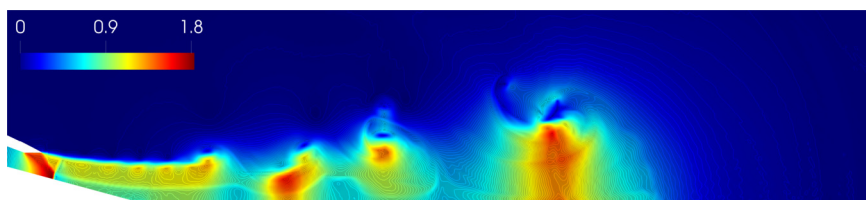


Fig. 29. Mach number of conical aerospike nozzle with NPR = 2.1.

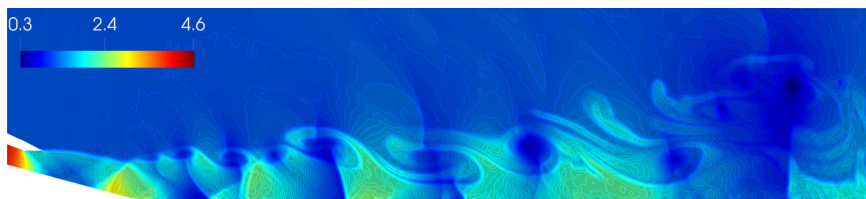


Fig. 30. Density of conical aerospike nozzle with NPR = 3.82.

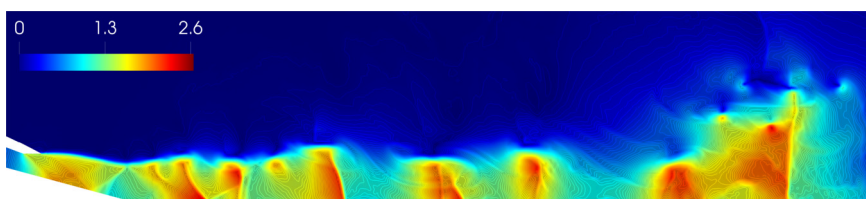


Fig. 31. Mach number of conical aerospike nozzle with NPR = 3.82.

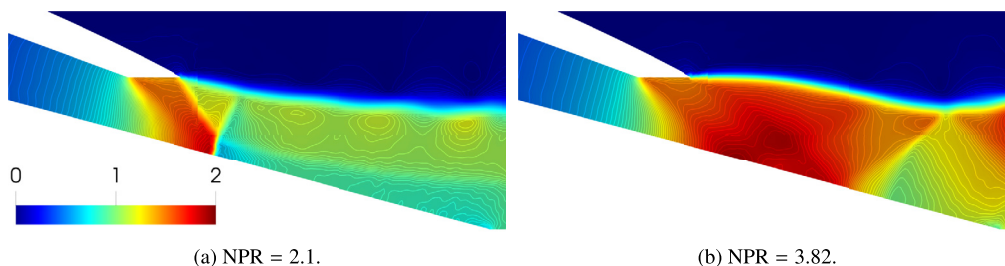


Fig. 32. Mach number at nozzle exit at $T = 2$ s, CFL = 0.8.

6. Conclusion

In this work, we present a hybrid high-resolution RBF-ENO method to reduce the overall computational complexity of the RBF-ENO method [21]. In the one-dimensional case, this method achieves the right order of convergence. We demonstrate the robustness of the two-dimensional hybrid high-resolution RBF-ENO method with several benchmarks as well as for two complex non-classical problems: the scramjet inflow problem and a conical aerospike nozzle jet simulation. To solve the conical aerospike nozzle simulation with the axisymmetric Euler equations, we describe a method to evaluate the source term with high-order accuracy. Furthermore, we introduce a positivity preserving limiter for non-polynomial reconstructions, which enables us to solve very challenging problems such as the scramjet inflow problem with Mach 10 inlet speed.

CRediT authorship contribution statement

Jan S. Hesthaven: Conceptualization, Funding acquisition, Supervision, Validation, Writing – review & editing. **Fabian Mönkeberg:** Conceptualization, Formal analysis, Methodology, Software, Visualization, Writing – original draft.

Declaration of competing interest

The authors declare that they have no known competing financial interests or personal relationships that could have appeared to influence the work reported in this paper.

Acknowledgements

This work has been supported by SNSF (513966).

References

- [1] S. Gottlieb, D.J. Ketcheson, C.-W. Shu, High order strong stability preserving time discretizations, *J. Sci. Comput.* 38 (2009) 251–289.
- [2] B. Van Leer, Towards the ultimate conservative difference scheme. V. A second-order sequel to Godunov's method, *J. Comput. Phys.* 32 (1979) 101–136.
- [3] C. Lanczos, *Discourse on Fourier Series*, Vol. 76, SIAM, 2016.
- [4] A. Harten, B. Engquist, S. Osher, S.R. Chakravarthy, Uniformly high order accurate essentially non-oscillatory schemes, III, *J. Comput. Phys.* 71 (1987) 231–303.
- [5] A. Harten, S.R. Chakravarthy, Multi-dimensional ENO schemes for general geometries, Technical Report 91-76, ICASE, 1991.
- [6] R. Abgrall, On essentially non-oscillatory schemes on unstructured meshes: analysis and implementation, *J. Comput. Phys.* 114 (1994) 45–58.
- [7] X.-D. Liu, S. Osher, T. Chan, Weighted essentially non-oscillatory schemes, *J. Comput. Phys.* 115 (1994) 200–212.
- [8] R.L. Hardy, Multiquadric equations of topography and other irregular surfaces, *J. Geophys. Res.* 76 (1971) 1905–1915.
- [9] A. Iske, *Approximation Theory and Algorithms for Data Analysis*, Springer, 2018.
- [10] M.D. Buhmann, Radial basis functions, *Acta Numer.* 2000 (9) (2000) 1–38.
- [11] G.E. Fasshauer, *Meshfree Approximation Methods with MATLAB*, Vol. 6, World Scientific, 2007.
- [12] G.E. Fasshauer, J.G. Zhang, On choosing “optimal” shape parameters for rbf approximation, *Numer. Algorithms* 45 (2007) 345–368.
- [13] T. Sonar, Optimal recovery using thin plate splines in finite volume methods for the numerical solution of hyperbolic conservation laws, *IMA J. Numer. Anal.* 16 (1996) 549–581.
- [14] A. Iske, T. Sonar, On the structure of function spaces in optimal recovery of point functionals for ENO-schemes by radial basis functions, *Numer. Math.* 74 (1996) 177–201.
- [15] T. Aboiyar, E.H. Georgoulis, A. Iske, High order WENO finite volume schemes using polyharmonic spline reconstruction, in: *Proceedings of the International Conference on Numerical Analysis and Approximation Theory NAAT2006*, Cluj-Napoca, Romania, Dept. of Mathematics, University of Leicester, 2006.
- [16] T. Aboiyar, E.H. Georgoulis, A. Iske, Adaptive ADER methods using kernel-based polyharmonic spline WENO reconstruction, *SIAM J. Sci. Comput.* 32 (2010) 3251–3277.
- [17] J. Guo, J.-H. Jung, A RBF-WENO finite volume method for hyperbolic conservation laws with the monotone polynomial interpolation method, *Appl. Numer. Math.* 112 (2017) 27–50.
- [18] C. Bigoni, J.S. Hesthaven, Adaptive WENO methods based on radial basis function reconstruction, *J. Sci. Comput.* 72 (2017) 986–1020.
- [19] J.S. Hesthaven, F. Mönkeberg, S. Zaninelli, RBF Based CWENO Method. *Spectral and High Order Methods for Partial Differential Equations ICOSAHOM 2018*, Springer, 2020, pp. 191–201.
- [20] J.S. Hesthaven, F. Mönkeberg, Entropy stable essentially nonoscillatory methods based on RBF reconstruction, *ESAIM: M2AN* 53 (2019) 925–958.
- [21] J.S. Hesthaven, F. Mönkeberg, Two-dimensional RBF-ENO method on unstructured grids, *J. Sci. Comput.* 82 (2020) 1–24.
- [22] G.-S. Jiang, C.-W. Shu, Efficient implementation of weighted ENO schemes, *J. Comput. Phys.* 126 (1996) 202–228.
- [23] B. Perthame, C.-W. Shu, On positivity preserving finite volume schemes for Euler equations, *Numer. Math.* 73 (1996) 119–130.
- [24] J. Duchon, *Splines Minimizing Rotation-Invariant Semi-Norms in Sobolev Spaces*, Springer, 1977, pp. 85–100.
- [25] C.A. Micchelli, Interpolation of scattered data: distance matrices and conditionally positive definite functions, *Constr. Approx.* 2 (1986) 11–22.
- [26] S.K. Godunov, A difference method for numerical calculation of discontinuous solutions of the equations of hydrodynamics, *Mat. Sb.* 89 (1959) 271–306.
- [27] J.S. Hesthaven, *Numerical Methods for Conservation Laws: From Analysis to Algorithms*, Society for Industrial and Applied Mathematics, 2017.
- [28] B. Gustafsson, The convergence rate for difference approximations to mixed initial boundary value problems, *Math. Comput.* 29 (1975) 396–406.
- [29] P. Buchmüller, C. Helzel, Improved accuracy of high-order WENO finite volume methods on Cartesian grids, *J. Sci. Comput.* 61 (2014) 343–368.
- [30] X. Zhang, C.-W. Shu, On maximum-principle-satisfying high order schemes for scalar conservation laws, *J. Comput. Phys.* 229 (2010) 3091–3120.
- [31] X. Zhang, C.-W. Shu, Maximum-principle-satisfying and positivity-preserving high-order schemes for conservation laws: survey and new developments, *Proc. R. Soc. Lond., Ser. A, Math. Phys. Eng. Sci.* 467 (2011) 2752–2776.
- [32] X. Zhang, Y. Xia, C.-W. Shu, Maximum-principle-satisfying and positivity-preserving high order discontinuous Galerkin schemes for conservation laws on triangular meshes, *J. Sci. Comput.* 50 (2012) 29–62.
- [33] X. Zhang, C.-W. Shu, On positivity-preserving high order discontinuous Galerkin schemes for compressible Euler equations on rectangular meshes, *J. Comput. Phys.* 229 (2010) 8918–8934.
- [34] P. Woodward, P. Colella, The numerical simulation of two-dimensional fluid flow with strong shocks, *J. Comput. Phys.* 54 (1984) 115–173.
- [35] C. Geuzaine, J. Remacle, Gmsh: a 3-d finite element mesh generator with built-in pre- and post-processing facilities, *Int. J. Numer. Methods Eng.* 79 (2009) 1309–1331.
- [36] F. Bisson, S. Nadarajah, D. Shi-Dong, Adjoint-based aerodynamic optimization of benchmark problems, in: *52nd Aerospace Sciences Meeting*, 2014, p. 1948.
- [37] C. Edwards, W. Small, J. Weidner, P. Johnston, Studies of scramjet/airframe integration techniques for hypersonic aircraft, in: *13th Aerospace Sciences Meeting*, 1975, p. 58.
- [38] C. Segal, *The Scramjet Engine: Processes and Characteristics*, Vol. 25, Cambridge University Press, 2009.
- [39] A.F. El-Sayed, *Fundamentals of Aircraft and Rocket Propulsion*, Springer, 2016.
- [40] A. Kumar, Numerical analysis of the scramjet inlet flow field using two-dimensional Navier-Stokes equations, in: *19th Aerospace Sciences Meeting*, 1981, p. 185.
- [41] A. Eberle, M. Schmatz, N. Bissinger, Generalized fluxvectors for hypersonic shock-capturing, in: *28th Aerospace Sciences Meeting*, 1990, p. 390.
- [42] K. Nakahashi, E. Saitoh, Space-marching method on unstructured grid for supersonic flows with embedded subsonic regions, *AIAA J.* 35 (1997) 1280–1285.
- [43] F. Alauzet, P.J. Frey, Estimateur d'erreur géométrique et métriques anisotropes pour l'adaptation de maillage. Partie II: exemples d'applications, Research Report RR-4789, INRIA, 2003, <https://hal.inria.fr/inria-00071797>.
- [44] J.S. Hesthaven, T. Warburton, *Nodal Discontinuous Galerkin Methods: Algorithms, Analysis, and Applications*, Springer Science & Business Media, 2007.
- [45] A. Mazaheri, C.-W. Shu, V. Perrier, Bounded and compact weighted essentially nonoscillatory limiters for discontinuous Galerkin schemes: triangular elements, *J. Comput. Phys.* (2019).
- [46] G. Mengaldo, D. De Grazia, F. Witherden, A. Farrington, P. Vincent, S. Sherwin, J. Peiro, A guide to the implementation of boundary conditions in compact high-order methods for compressible aerodynamics, in: *7th AIAA Theoretical Fluid Mechanics Conference*, 2014, p. 2923.
- [47] M.J. Turner, *Rocket and Spacecraft Propulsion: Principles, Practice and New Developments*, Springer Science & Business Media, 2008.
- [48] T. Ito, K. Fujii, Numerical analysis of the base bleed effect on the aerospike nozzles, in: *40th AIAA Aerospace Sciences Meeting & Exhibit*, 2002, p. 512.

- [49] M. Nazarinia, A. Naghib-Lahouti, E. Tolouei, Design and numerical analysis of aerospike nozzles with different plug shapes to compare their performance with a conventional nozzle, in: AIAC-11 Eleventh Australian International Aerospace Congress, 2005.
- [50] N. Zeoli, S. Gu, Computational validation of an isentropic plug nozzle design for gas atomisation, *Comput. Mater. Sci.* 42 (2008) 245–258.
- [51] S. Eilers, W. Matthew, S. Whitmore, Analytical and experimental evaluation of aerodynamic thrust vectoring on an aerospike nozzle, in: 46th AIAA/ASME/SAE/ASEE Joint Propulsion Conference & Exhibit, 2010, p. 6964.
- [52] S. Sanoob, M. Prince, B. Sundar, Numerical analysis of aero-spike nozzle for spike length optimization, *Int. J. Res. Eng. Technol.* 1 (2013) 1–14.
- [53] M. Propst, J. Sieder, C. Bach, M. Tajmar, Numerical analysis on an aerodynamically thrust-vectorized aerospike nozzle, in: Proceedings of the 63rd German Aerospace Congress (DGLR), Augsburg, 2014.
- [54] S.B. Verma, Performance characteristics of an annular conical aerospike nozzle with freestream effect, *J. Propuls. Power* 25 (2009) 783–791.
- [55] M. He, L. Qin, Y. Liu, Numerical investigation of flow separation behavior in an over-expanded annular conical aerospike nozzle, *Chin. J. Aeronaut.* 28 (2015) 983–1002.
- [56] Y. Ji, M. He, H. Liu, Reynolds number influence on the backpressure-induced shock–boundary layer interaction in an asymmetric supersonic expansion flow, *Aerosp. Syst.* (2019) 1–8.
- [57] P.P. Nair, A. Suryan, H.D. Kim, Computational study on flow through truncated conical plug nozzle with base bleed, *Propuls. Power Res.* (2019).
- [58] A. Bernard-Champmartin, J.-P. Braeunig, J.-M. Ghidaglia, An Eulerian finite volume solver for multi-material fluid flows with cylindrical symmetry, *Comput. Fluids* 83 (2013) 170–176.
- [59] D. Dunavant, High degree efficient symmetrical Gaussian quadrature rules for the triangle, *Int. J. Numer. Methods Eng.* 21 (1985) 1129–1148.